LEIBNIZ-INSTITUT
FÜR
ATMOSPHÄREN
PHYSIK

INAUGURAL-DISSERTATION

am Leibniz-Institut für Atmosphärenphysik in Kühlungsborn
zur Erlangung der Doktorwürde
der Mathematisch-Naturwissenschaftlichen Fakultät
der Universität Rostock

Gravity waves and momentum fluxes in the mesosphere and lower thermosphere region

von
Manja Placke

Abstract: Gravity waves propagating through the Earth's atmosphere play an important role for the coupling between different atmospheric layers as they actively transport momentum and energy away from their source regions and deposit it when dissipating. The objective of this thesis is to investigate the interactions between gravity wave momentum fluxes and the background wind field in the mesosphere and lower thermosphere region at polar and midlatitudes. Also, the underlying linear theory of gravity waves and the momentum balance are tested. For these purposes data of different radar instruments with different applied analysis methods is used and simultaneous radar and lidar measurements are analyzed. The use of a mechanistic general circulation model allows the test of the applied methods and of the underlying linear gravity wave theory as well as the evaluation of the observational results.

Postal address:
Schloss-Str. 6
18225 Ostseebad Kühlungsborn
Germany

IAP Kühlungsborn
Februar 2014
IAP Nr. 36/2014
ISSN 1615–8083

LEIBNIZ-INSTITUT
FÜR
ATMOSPHÄREN
PHYSIK

Gravity waves and momentum fluxes in the mesosphere and lower thermosphere region

von
Manja Placke

Dieser Forschungsbericht wurde als kumulative Dissertation von der Mathematisch-Naturwissenschaftlichen Fakultät der Universität Rostock angenommen.

Gutachter:	Prof. Dr. M. Rapp (Ludwig-Maximilians-Universität München)
	Prof. Dr. M. Riese (Bergische Universität Wuppertal)

eingereicht am: 20. September 2013
verteidigt am: 21. Februar 2014

Summary

Gravity waves propagating through the Earth's atmosphere play an important role for the coupling between different atmospheric layers as they actively transport momentum and energy away from their source regions and deposit it when dissipating. The objective of this thesis is to investigate the interactions between gravity wave momentum fluxes and the background wind field in the mesosphere and lower thermosphere region at polar and midlatitudes. Also, the underlying linear theory of gravity waves and the momentum balance are tested. For these purposes data of different radar instruments with different applied analysis methods is used and simultaneous radar and lidar measurements are analyzed. The use of a mechanistic general circulation model allows the test of the applied methods and of the underlying linear gravity wave theory as well as the evaluation of the observational results.

Zusammenfassung

Schwerewellen breiten sich durch die Erdatmosphäre aus und spielen eine bedeutende Rolle bei der Kopplung unterschiedlicher Atmosphärenschichten, da sie aktiv Impuls und Energie aus ihren Quellregionen wegtransportieren und fernab bei ihrer Dissipation ablagern. Das Ziel dieser Dissertation ist die Untersuchung der Wechselwirkungen zwischen Schwerewellenimpulsflüssen und dem Hintergrundwindfeld in der Mesosphäre und unteren Thermosphäre in polaren und mittleren geographischen Breiten. Zudem werden die zugrunde liegende lineare Schwerewellentheorie und das Impulsgleichgewicht überprüft. Für diese Zwecke werden Messdaten verschiedener Radargeräte unter Anwendung unterschiedlicher Analyseverfahren verwendet sowie simultane Radar- und Lidarmessungen ausgewertet. Die Nutzung eines mechanistischen globalen Zirkulationsmodells ermöglicht die Überprüfung der angewandten Methoden und der zugrunde liegenden linearen Schwerewellentheorie sowie die Validierung der Messergebnisse.

Contents

1 Properties and importance of atmospheric gravity waves **1**

2 State of the art and objectives of this thesis **4**

3 Theory: Gravity waves and their effects on the mean flow **8**

3.1 Linear theory of gravity waves 8
3.2 Gravity wave – mean flow interactions 11
3.3 Atmospheric modeling with KMCM 13

4 Experimental Methods **15**

4.1 Measurements with radar and lidar 15
4.2 Determination of gravity wave activity and momentum fluxes 19

5 Results **22**

5.1 Paper I (*Placke et al.*, 2011a): Gravity wave momentum fluxes in the MLT– Part I: Seasonal variation at Collm (51.3°N, 13.0°E) 22
5.2 Paper II (*Placke et al.*, 2011b): Gravity wave momentum fluxes in the MLT– Part II: Meteor radar investigations at high and midlatitudes in comparison with modeling studies 25
5.3 Paper III (*Placke et al.*, 2013): Testing linear gravity wave theory with simultaneous wind and temperature data from the mesosphere 29
5.4 Paper IV (Unpublished manuscript): Mesospheric gravity wave momentum fluxes from radar measurements at polar latitudes in comparison with model results 34

6 Conclusions and outlook **37**

Bibliography **40**

A Table **47**

B List of included publications and manuscripts **48**

Chapter 1

Properties and importance of atmospheric gravity waves

The Earth's atmosphere is a mantle of air encompassing our planet like a thin protective film and separating it from outer space. The atmosphere is of vital importance for the existence of life on Earth owing to the variety of physical processes which take place in it and determine, among others, what we summarize as weather. Basically these processes are driven by the energy input from the sun and are for instance co-determined by the rotation of the Earth (Coriolis force), by the latitude, land-sea-arrangement, orography and other geophysical factors. The motion of air in the atmospheric system leads to the formation of different kinds of waves with different spatial and temporal scales. They can for example be identified by wind and density/temperature fluctuations. The most important wave types are Rossby waves, thermal tides, equatorial waves, and internal gravity waves. Rossby waves with the latitudinal variation of the Coriolis force as restoring force and thermal tides generated by differential solar heating are both of planetary extent. The same applies to equatorial waves which are trapped close to the equator. Locally generated gravity waves have smaller dimensions and are mainly restored by buoyancy. All these waves are mainly forced in the lowermost part of the atmosphere (the troposphere), propagate vertically and horizontally and dissipate in different altitude regions.

The vertical structure of the Earth's atmosphere with its layers up to around 100 km altitude, separated by changing signs of the temperature gradient, is schematically shown in Fig. 1.1 (left). The vertical profile of the temperature at polar latitudes (70°N) for summer (red) and winter (blue) has been taken from CIRA-86 (COSPAR International Reference Atmosphere 1986, *Fleming et al.*, 1990). The troposphere ranging up to 10–12 km height is characterized by a temperature decrease from ~280 K at ground level to ~230 K at the tropopause in summer. The tropopause is the transition region to the overlying stratosphere. In the stratosphere the presence of ozone results in the absorption of solar UV radiation converting the electromagnetic radiation into heat and thus increasing the temperature up to about 280 K (in summer) around 50 km where the stratopause lies. Above that altitude, the mesosphere follows with decreasing temperature up to the mesopause around 90 km. There, the temperature minimum of the atmosphere occurs with values down to ~130 K in summer before the temperature increases again in the thermosphere due to photolysis of molecular oxygen (O_2).

The region between about 60 to 110 km is labeled as the MLT (mesosphere and lower thermosphere) region. It is characterized by a residual circulation from the summer to the winter pole around mesopause heights (see, e. g., *Holton and Alexander*, 2000) which leads to two outstanding features of the polar summer mesopause: 1) gravity waves break at mesopause heights which is associated with momentum deposition leading to a closure of the mesospheric wind jet and a reversal of the zonal wind (e. g., *Manson et al.*, 2004)

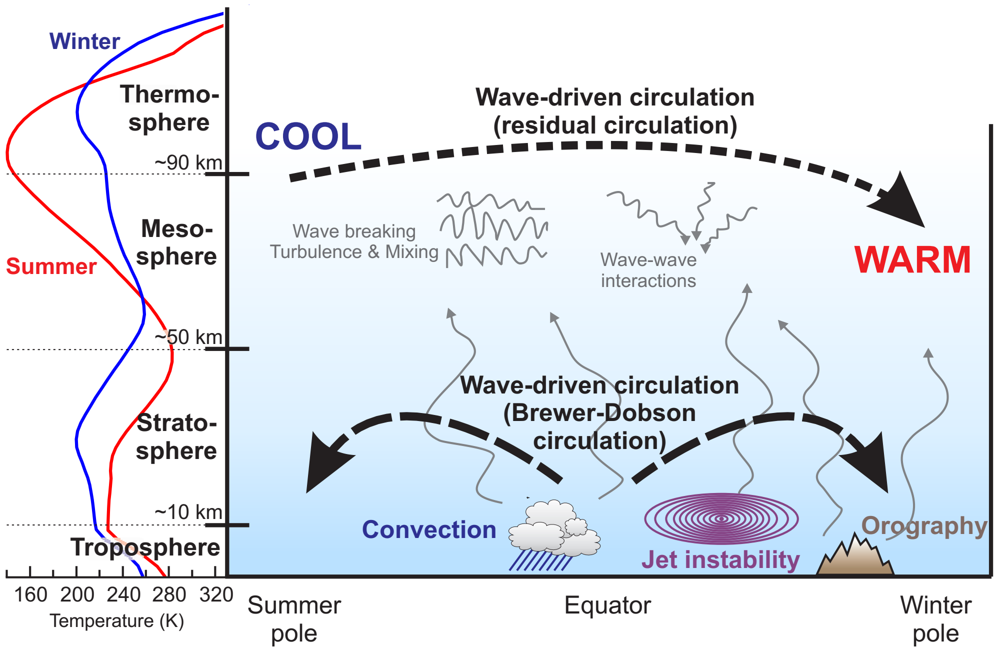

Figure 1.1: Schematic showing the atmospheric layers as related to the temperature gradients and the vertical profile of the temperature at polar latitudes in summer (June) and winter (December) after CIRA-86 (left). Also shown is an overview of atmospheric wave sources and propagation as well as the wave-driven circulations (right).

and 2) the summer temperature minimizes to values of $\sim$130 K around 88 km (e. g., *von Zahn and Meyer*, 1989; *Lübken*, 1999) as the residual circulation causes an upward transport of air masses in the region of the summer pole and thus leads to an adiabatic cooling of the air. This temperature minimum is approximately 100 K cooler than the hypothetical radiative equilibrium temperature at the same altitudes. Conversely, the downward transport of air masses at the winter pole leads to adiabatic heating (see Fig. 1.1, right). Hence, the mesopause is considerably (by approximately 60–70 K) cooler in summer than in winter (e. g., *Lübken and von Zahn*, 1991).

From all this it is obvious that gravity waves (GW) are of utmost importance for the dynamics and structure of the middle atmosphere. GW are oscillations of air parcels with buoyancy as the restoring force. The main tropospheric sources of GW are the airflow over the orography (mountains), vertical movement in convection cells as well as jet instabilities in connection with frontal zones which are associated with strong wind shears. Furthermore, wave-wave interactions and superposition of different waves in different atmospheric regions can also generate GW. These sources are schematically shown in Fig. 1.1 (right).

After their generation, GW propagate vertically and horizontally with typical vertical wavelengths of 5 to 15 km and horizontal wavelengths of 10 km to several 100 km which corresponds to wave periods of some minutes up to several hours. Typical horizontal phase speeds are on average $\sim$30 to 40 m/s and can reach values up to 80 m/s (e. g., *Andrews et al.*, 1987). For vertically propagating GW, the intrinsic frequency relative to the background wind is limited by the inertia or Coriolis frequency and the Brunt-Väisälä frequency N (or buoyancy frequency). The Coriolis frequency ($f = 2\,\Omega \cdot \sin\Phi$, with Ω being the angular velocity of the Earth and Φ being the latitude) corresponds to periods between about 12 and 15 h at polar and midlatitudes, respectively. The Brunt-Väisälä frequency N corresponds to periods of $\sim$5 min in the upper mesosphere (e. g., *Fritts and Alexander*, 2003). While propagating, GW actively transport momentum and energy from their source regions to the middle and upper atmosphere thus playing an important role for the coupling between different atmospheric layers. Thereby, GW can mainly only propagate upward when they move against the background wind field.

With increasing height, the GW amplitudes grow exponentially due to the air density decrease. Consequently, a considerable fraction of GW breaks at upper mesospheric heights. In the dissipation process, they deposit their momentum and energy onto the background atmosphere and influence the wind field by accelerating or decelerating the mean zonal flow. Thereby, they may even reverse whole wind regimes. This GW–mean flow interaction drives the residual mesospheric summer-to-winter-pole circulation which is schematically shown in Fig. 1.1 (right) and accounts for the strong departures from radiative equilibrium in the MLT region. Also, GW make a small contribution to the stratospheric Brewer-Dobson circulation which is mainly driven by planetary waves and is the equator-to-pole circulation describing the mean meridional mass transport in the stratosphere with ascending air in the tropics, poleward flow and descent in the polar regions. In addition, unstable GW generate turbulence and mixing whereby GW are also most important for the distribution of trace gases.

Importantly, the above implies that the mesopause region is dependent on tropospheric variability due to the excitation and propagation processes of GW. Furthermore, especially short- and meso-scale GW contribute largely to the momentum balance of the stratosphere and dominate in the mesosphere (e. g., *Fritts and Alexander*, 2003; *Ern et al.*, 2004).

The investigation of GW, their annual activity variation and their related momentum fluxes in the MLT region as well as the mentioned interactions between GW and the mean flow are subject of this thesis. Also, linear GW theory is tested in case studies and the momentum balance is investigated. Therefor, different instruments for atmospheric monitoring are used – primarily different radar instruments at high and midlatitudes, but also lidar instruments. The combination of radar wind and lidar temperature measurements allows the validation of the polarization relations based on linear GW theory. Various radars provide results at different geographical locations and make comparisons of winds and momentum fluxes from different analysis methods possible. Additionally, model data is used for testing and evaluating the applied methods and the underlying linear theory. The model data also allows comparisons with observational data and an evaluation of the results from the measurements.

This thesis is organized as follows. In Chapter 2, the state of the art and the objectives of this thesis are presented. In Chapter 3, the linear theory of GW and their effects on the mean flow are shortly discussed. Also, the atmospheric modeling with the GW-resolving model KMCM (Kühlungsborn Mechanistic general Circulation Model) is introduced. Chapter 4 describes the experimental methods, i. e., measurements with radar and lidar instruments are explained and methods for the determination of GW activity and GW momentum fluxes used for this work are presented. Chapter 5 then summarizes the key results of this cumulative thesis giving an overview of the three published papers *Placke et al.* (2011a,b, 2013) and one yet unpublished manuscript which are to be found in the Appendix. Finally, the most important results are summarized and ideas for future work are outlined in Chapter 6.

Chapter 2

State of the art and objectives of this thesis

Atmospheric GW belong to those types of waves which are of greatest importance for the large-scale behavior of the middle atmosphere (*Andrews et al.*, 1987) as they crucially influence the structure, dynamics, and variability of this atmospheric region (e. g., *Fritts and Alexander*, 2003). Also, they are relevant for the coupling between different atmospheric layers from the troposphere to the MLT region as they transport momentum and energy from their source regions through the atmosphere and deposit it when breaking at higher altitudes. GW exist due to buoyancy restoring forces in a stably stratified atmosphere and move vertically and horizontally. The experimental characterization of GW is challenging due to their vertical and horizontal extents which actually require large observation volumes and a sufficient time resolution to resolve the wave periods and duration. Furthermore, observations in the stratosphere and lower mesosphere are rare at present.

Historically seen, the interpretation of atmospheric motions in terms of GW was first suggested by *Hines* (1960). However, the acceptance of GW as a main driver of the middle atmosphere first began in the 1980s. For instance *Lindzen* (1981) and *Holton* (1982) investigated the effects of GW on the general circulation of the middle atmosphere. *McLandress* (1998) published a tutorial showing the impact of small-scale GW on the large-scale circulation and discussed the parameterization of GW in general circulation models. Later, *Fritts and Alexander* (2003) gave a thorough review of GW at different scales as well as their impact on the middle atmosphere. From a variety of publications it is known that GW, especially the GW momentum flux, greatly influence the background state of the middle atmosphere. So they cause the very low temperatures in the summer mesopause and drive the upper mesospheric summer zonal wind reversal.

To broaden the understanding and knowledge about GW, it is important and essential to investigate the activity of GW and their annual variation as well as the variability and strength of GW momentum fluxes and their possible effects onto the background mean flow. There exists a variety of instruments and analysis methods to derive GW activity and momentum fluxes from observations. However, it is important as well to evaluate such analysis methods by the use of model data. Furthermore, it is essential to test the underlying linear theory of GW, to investigate their kinetic and potential energy and to examine the mesospheric momentum balance which is strongly affected by short- and meso-scale GW. Investigations at different locations and latitudes help to get a comprehensive picture of GW and their global properties.

Currently used instruments for GW measurements have different benefits and drawbacks. Rockets for instance measure the vertical structure of the mesosphere in situ with high resolution (e. g., turbulent energy dissipation rates from neutral air density fluctuations by *Rapp et al.*, 2004), but can give no significant information about horizontal structures. Moreover, rocket flights are very expensive, are performed infrequently and measure only in very limited time intervals. The latter also applies for radiosondes which measure in the tropo- and lower stratosphere (e. g., GW activity studies by *Allen and Vincent*, 1995) or falling spheres which cover approximately the height range from 95 to 35 km (e. g., temperature and density measurements by *Lübken*, 1999). Measurements with these instruments are done in situ with high vertical resolution as well, but are mainly conducted sporadically on a campaign basis.

Satellites like CRISTA[1] (e. g., *Eckermann and Preusse*, 1999) or TIMED[2] with the SABER[3] instrument (e. g., *Krebsbach and Preusse*, 2007) allow analyses of GW activity and can give global GW climatologies based on GW temperature variances (see *Preusse et al.*, 2006). *Ern et al.* (2004) presented global maps of indirectly retrieved GW momentum fluxes from CRISTA satellite observations in the stratosphere (25 km height) and recently *Ern et al.* (2011) presented global GW momentum fluxes up to the MLT region for the first time. Also, *Wright and Gille* (2011) published stratospheric GW momentum fluxes (16–60 km height) and their strong relationship with monsoons from observations with HIRDLS[4] on the Aura satellite. In a further study by *Schmidt et al.* (2008), the global GW activity expressed by the specific potential energy has been investigated from GPS[5] radio occultation data from the CHAMP[6] satellite in the tropopause region. Hence, satellite measurements cover a big altitude range, but until now the propagation direction of the waves cannot be defined, i. e., only absolute values of momentum flux based on temperature fluctuations are available. Furthermore, the coarse resolution of satellite observations leads to limitations in resolving the whole spectrum of GW (*Alexander et al.*, 2002). Another considerable influence limiting the observable GW spectrum arises from the "observational filter" (e. g., *Alexander*, 1998) or "visibility filtering" (e. g., *Preusse et al.*, 2006) which implies that instruments or measurement techniques are sensitive only to a certain part of the total GW spectrum and hence select GW with certain horizontal and vertical wavelengths.

Lidar instruments can cover a broad height range by combination of different lidar systems (e. g., *Rauthe et al.*, 2006) and measure temperatures derived from background density. GW can be identified by temperature fluctuations and the seasonal variation of GW activity can be observed (*Rauthe et al.*, 2008; *Gerding et al.*, 2008). But as lidar measurements are frequently restricted to nighttime and cloudfree conditions, the temporal coverage of lidar systems is far from ideal and data gaps need to be closed by using different techniques.

Radar measurements are limited to certain height regions: to the troposphere and lower stratosphere as well as to the mesospheric and lower thermospheric region. Their big advantage is, that they are able to monitor wind variations and GW activity continuously (e. g., *Manson et al.*, 2002; *Gavrilov et al.*, 2002; *Jacobi et al.*, 2006; *Hoffmann et al.*, 2010) as they can be operated independently from weather conditions. Also, GW momentum fluxes can be directly measured (e. g., *Vincent and Reid*, 1983; *Fritts and Janches*, 2008; *Fritts et al.*, 2012). Consequently, radars can observe the annual cycle of the wind field and the GW activity in detail, especially in the mesopause region which is – beside the tropopause region – one of the very interesting parts of the atmosphere for GW breaking and GW–mean flow interactions. These processes will be discussed in detail in Chapter 3.

Basic types of atmospheric radar for investigations in the MLT region are medium frequency (MF) radars operating at a frequency of about 0.3 – 3.2 MHz and very high frequency (VHF) radars operating at 30 – 300 MHz which include meteor radars. MF radars have contributed unique climatological information at different latitudes since the 1970s and cover a height range from 60/80 to 100 km (day/night) (e. g., *Manson et al.*, 1997) depending on

[1] CRISTA = Cryogenic Infrared Spectrometers and Telescopes for the Atmosphere
[2] TIMED = Thermosphere Ionosphere Mesosphere Energetics and Dynamics
[3] SABER = Sounding of the Atmosphere using Broadband Emission Radiometry
[4] HIRDLS = High Resolution Dynamics Limb Sounder
[5] GPS = Global Positioning System
[6] CHAMP = Challenging Minisatellite Payload

the ionization of the atmosphere due to the incidence of sunlight. Mostly, MF radars use spaced-antenna (SA) and interferometry methods for analysis. With the SA method, the mesospheric wind field can be estimated from signals which are received at spatially separated radar antennas by applying correlation techniques (e. g., *Briggs*, 1984). Interferometry methods use electromagnetic waves with different well-defined frequencies to get information about three-dimensional scatter structures in the atmosphere from phase differences. Winds, layered phenomena, activity of different kinds of waves and their effects on their background have been investigated in many previous studies such as in *Manson et al.* (1999), *Hoffmann et al.* (2002), *Riggin et al.* (2003) or *Hoffmann et al.* (2008) and the many references therein.

Only few MF radars also have a Doppler beam steering (DBS) capability (see, e. g., *Reid and Vincent*, 1987). The DBS technique uses narrow radar beams tilted to certain directions and combines all signals received with the whole antenna array as one receiving signal for each tilt direction. By making use of the Doppler effect, the radial wind velocity can be estimated for each individual direction. The combination of the radial wind velocities of at least three different directions allows the calculation of the three-dimensional wind vector (e. g., *Woodman and Guillen*, 1974; *Zecha*, 1999). A drawback of DBS capable MF radars is that they require very large antenna arrays and hence higher costs and more technical effort. Nevertheless, their big advantage is that – in contrast to smaller MF radars – they can form narrower beams and give more detailed information about momentum fluxes in the MLT region.

VHF radars for investigations in the middle atmosphere are mesosphere-stratosphere-troposphere (MST) radars and meteor radars. Measurements with meteor radars operating in the VHF band reach back to the 1950s when radio Doppler techniques were introduced to study the drift of meteor trails moving with the background wind and thus determining winds at altitudes between about 80 and 100 km. But the greatest difficulty was the determination of the azimuth directions of the meteor echoes. Since the late 1970s, narrow beam VHF radars were also used for meteor studies. But as these radars were often optimized for studies in the meso-, strato- and troposphere, the meteor count rates at meteor ablation heights were low. An overview of the history of meteor studies can for instance be found in *Elford* (2001) and an excellent review on meteor phenomena and bodies and their observations since the late 19th century is given by *Ceplecha et al.* (1998). Since the 1990s, meteor radars rather use interferometric techniques thus having a wider beam and measuring meteors almost over the whole sky (so-called "all-sky" systems). The latest meteor radar system, the all-sky interferometric (SKiYMET) meteor radar, was developed around the turn to the 21st century (*Hocking et al.*, 2001). It allows real-time meteor detections and extensive analysis routines thanks to sophisticated computer technique. With this type of meteor radar, the wind field as well as wind variances and momentum fluxes of short period GW around mesopause heights can be obtained simultaneously with an analysis method proposed by *Hocking* (2005). With another technique, *Mitchell and Beldon* (2009) and *Beldon and Mitchell* (2009) determined variances of horizontal wind velocities as a proxy for the activity of the GW field from all-sky meteor radars by using the scatter of individual meteor drift velocities. MST radars which are wind-profiling systems can also be used for the investigation of meteors, but this application is confined to individual case studies as for instance done by *Tsuda et al.* (1985).

For certain purposes, simultaneous measurements of wind and temperature are required. This for instance concerns the check of the linear GW theory, more precisely the polarization relations between wind and temperature variations, or the investigation of the kinetic and potential energy of GW in their upward propagation and breaking process. For the lower atmosphere, radiosondes can be used for such examinations as for instance shown by *Geller and Gong* (2010). In the mesosphere and mesopause region, instruments with the ability to measure both wind and temperature are rare. Notably, *Baumgarten* (2010) reported the first simultaneous Rayleigh lidar temperature and wind measurements in the strato- and mesosphere. Apart from that, often the combination of different instruments is necessary to obtain winds and temperatures at the same time as for instance done by *Suzuki et al.* (2010) who used airglow, lidar and radar measurements in Japan.

With all the mentioned instruments above, various properties of GW can be obtained in different ways. Also, the use of several instruments at different locations is advantageous to compare results of different analysis methods and at different latitudes. This gives a comprehensive picture of GW, their global occurrence, properties and effects on their background.

The objective of this thesis is to investigate the annual variation of horizontal winds and GW momentum fluxes at polar and midlatitudes in order to get an insight into the coupling processes between GW and the background circulation in the MLT region. Therefor, results of different analysis methods applied to different types of radar are considered with respect to their benefits and drawbacks. Linear theory of GW is tested by verification of the polarization relations between simultaneous mesospheric radar wind and lidar temperature measurements and by verification of the momentum balance. Moreover, a GW-resolving model is used for testing the used methods and the underlying GW theory and for evaluating the results.

Chapter 3

Theory: Gravity waves and their effects on the mean flow

3.1 Linear theory of gravity waves

GW owe their existence to buoyancy as the restoring force in a stably stratified atmosphere. This means if an air parcel is displaced from its equilibrium state in a stably stratified atmosphere it starts adiabatic oscillations around its equilibrium level. The atmospheric motions due to the GW can for instance be observed as wind and density or temperature variations. The relationships between the magnitudes of the wind and temperature oscillations are referred to as "polarization relations" which form the basis of the linear theory. The first mentioning of these polarization relations as relations between wave perturbation quantities was done by *Hines* (1960) and later specified by *Gossard and Hooke* (1975). Also, the kinetic and potential energy of the GW can be derived from the wind and temperature variations. Hence, vertical profiles of wind and temperature observations can be analyzed with respect to their agreement with expectations from linear wave theory. It must be noted that the applicability of the linear theory to mesospheric observations is difficult since for theoretical considerations it is usually assumed that only a single monochromatic wave exists. In contrast, atmospheric observations typically reveal a spectrum of waves due to superposition (e. g., *Lue and Kuo*, 2012) and non-linear interactions (e. g., *Wüst and Bittner*, 2006).

To determine the polarization relations and hence to test linear GW theory, different algorithms can be used. *Eckermann* (1996) for instance did a comparison of different analysis methods in order to find out their benefits and drawbacks as well as the relationships between them. The most straight forward case is taking filtered wind and temperature time series directly from instrumental observations and determining the deviations of these parameters from a mean value. Thus, the relation between temperature variations T' and wind variations in zonal (u') or meridional (v') direction can be calculated, i. e., values for T'/u' and T'/v' can be obtained.

Knowing the characteristics (parameters) of the wave itself, the ratio of T' to the vertical mean temperature T_m is for instance given by

$$\frac{T'}{T_m} = i\frac{N^2(k^2 + l^2)}{mg} \cdot \frac{1}{\omega k + ilf} \cdot u' \tag{3.1}$$

(see, e. g., *Zink*, 2000). Here i is the imaginary unit, N is the Brunt–Väisälä frequency, k, l and m are the wave numbers in zonal, meridional and vertical direction, respectively, g is the gravitational acceleration, and ω and f are the intrinsic and the Coriolis frequency, respectively. The Brunt-Väisälä frequency, or buoyancy frequency, is the frequency at which a vertically displaced air parcel oscillates within a statically stable environment and thus provides a useful description of atmospheric stability. It varies with height and can be calculated for a certain altitude interval as

$$N^2 = \frac{g}{T}\left(\frac{g}{c_p} + \frac{\partial T}{\partial z}\right) \ . \tag{3.2}$$

Here, c_p is the specific heat capacity of air at constant pressure and z is the vertical height coordinate. Typical values of the squared Brunt-Väisälä frequency are $\sim 5 \cdot 10^{-4}\, s^{-2}$ in the stratosphere and $3 \cdot 10^{-4}\, s^{-2}$ in the mesosphere (*Andrews et al.*, 1987). From simple conversion of Eq. 3.1, the polarization relation between temperature and zonal wind variation can be obtained:

$$\frac{T'}{u'} = i\frac{N^2(k^2+l^2)}{mg} \cdot \frac{T_m}{\omega k + ilf} \ . \tag{3.3}$$

By considering the ratio of the zonal to the meridional wind fluctuation

$$v' = \frac{l\omega - ikf}{k\omega + ilf} \cdot u' \ , \tag{3.4}$$

the polarization relation between temperature and meridional wind variation is:

$$\frac{T'}{v'} = i\frac{N^2(k^2+l^2)}{mg} \cdot \frac{T_m}{\omega l - ikf} \ . \tag{3.5}$$

Hence, the polarization relations can also be determined from the right hand sides of Eqs. 3.3 and 3.5 by using measurements of the mean background temperature and by estimating the wave numbers and intrinsic frequency which can be calculated by hodograph and Stokes parameters analysis from wind data.

The hodograph analysis is a commonly used method to retrieve GW characteristics from vertical profiles of zonal and meridional wind fluctuations. The hodograph is obtained by plotting the height vectors of v' and u' at a specific time against each other which often results in an ellipse for inertia GW (e. g., *Cot and Barat*, 1986). One of the first applications of the hodograph analysis to mesospheric GW was done by *Muraoka et al.* (1994). *Hall et al.* (1995) applied a method of hodograph analysis to investigate the propagation characteristics of long period GW (periods from 2 to 10 hours) by using three MF radars. Parameters that can be derived from the hodograph analysis are the vertical sense of the GW propagation (from the rotational sense of the ellipse), the direction of the horizontal wave propagation (which is parallel to the major axis of the ellipse), the vertical wavelength, and the intrinsic frequency (from the ratio of the major to the minor axis of the ellipse). For the northern hemisphere, a clockwise rotation of the hodograph indicates upward GW propagation. The horizontal propagation direction can be estimated with an uncertainty of 180°. This uncertainty can be resolved by using the polarization relations between u', v', and T'. The determination of the wave numbers can be done by first fixing the vertical wavelength by means of a rotary-spectra analysis of the wind data, and then using the Doppler relation

$$k_h = \frac{\omega_{obs} - \omega}{\overline{u_h}} \tag{3.6}$$

and the dispersion relation for inertia GW (with $N^2 \gg \omega^2$):

$$\omega^2 = f^2 + \frac{N^2 k_h^2}{m^2} \ . \tag{3.7}$$

Here, k_h is the horizontal wave number, ω_{obs} is the observed frequency and $\overline{u_h}$ is the mean horizontal wind in the direction of the wave propagation. From the intrinsic frequency ω and the horizontal wave number k_h, the horizontal phase velocity c_{Ph} of a wave can be calculated by $c_{Ph} = \omega/k_h$. That is the velocity at which the phase of any frequency component of a wave moves.

In summary, the hodograph analysis is a straightforward technique for determining the parameters which are required to evaluate the right hand side of the polarization relations (Eqs. 3.3 and 3.5). An important constraint which needs to be noted is that the hodograph analysis is based on the assumption of a single dominating monochromatic wave which is present at a particular time in a region of minimal background wind shear. In reality, however, there are frequently a number of waves with different periods which are superposed during the observation.

As a suitable method for such cases, the Stokes parameters analysis enables a description of the state of polarization of a GW field with strong amplitudes during a certain time interval statistically. This method is some kind of generalization of the hodograph analysis. It had been introduced by *Vincent and Fritts* (1987) showing that GW motions in the mesosphere follow certain regularities which can only be explained if the waves are partially polarized, a phenomenon which is for instance well known for electromagnetic waves (e. g., *Hecht*, 2001). *Eckermann and Vincent* (1989) extended the analysis by *Vincent and Fritts* (1987) in the spectral domain. As for the hodograph analysis, vertical profiles of the zonal and meridional wind fluctuations are considered to calculate the Stokes parameters. These are the total variance $I = \overline{u'^2} + \overline{v'^2}$, the axial anisotropy (or variance difference) $D = \overline{u'^2} - \overline{v'^2}$, the in-phase component of the complex correlation between the wave components (or "in-phase" covariance) $P = 2\overline{u'v'}$ which is associated with linear polarization, and the "in quadrature" covariance $Q = \overline{\widehat{u}\widehat{v}\sin\delta}$ which is associated with circular wave polarization. Here $\widehat{u}$ and $\widehat{v}$ are the peak amplitudes of u' and v' and δ is the polarization angle which is the difference between the respective phases of the wind field in zonal and meridional direction. For $\delta = 0°$ or $180°$ linear polarization is present, $\delta = 90°$ or $270°$ implies circular polarization. Anything between those values implies elliptical polarization. Overbars indicate vertical averages over the full wave period in height. The sum of the horizontal wind variances I is a measure of the GW activity. From the Stokes parameters, the degree of wave polarization d between zonal and meridional wind fluctuation can be calculated as

$$d = \frac{(D^2 + P^2 + Q^2)}{I} \, . \tag{3.8}$$

The averaged axial ratio of the wave ellipse is given as

$$R = \tan\mu \tag{3.9}$$

with

$$\mu = \frac{1}{2} \cdot \arcsin\left(\frac{Q}{d \cdot I}\right) . \tag{3.10}$$

The wave propagation direction can be determined by

$$\Theta = \frac{1}{2} \cdot \arctan\left(\frac{P}{D}\right) . \tag{3.11}$$

From the axial ratio R, the intrinsic frequency ω is obtained by the relation $\omega = f/R$. The horizontal and vertical wave numbers k_h and m can be estimated from the Doppler and dispersion equation (Eqs. 3.6 and 3.7). With the wave orientation Θ, k_h can be separated into the zonal and meridional wave number k and l. With this formalism at hand, linear wave theory can be tested straight forwardly by independently evaluating (and comparing) the left and right hand sides of Eqs. 3.3 and 3.5.

A further test of linear GW theory can be performed by considering vertical profiles of kinetic and potential energy and their relation to each other. The kinetic energy E_{kin} per unit mass is obtained from the wind variations in zonal and meridional direction:

$$E_{kin} = \frac{1}{2}\overline{(u'^2 + v'^2)}. \tag{3.12}$$

The potential energy E_{pot} per unit mass is determined by temperature variations and the mean temperature per height $\overline{T}$:

$$E_{pot} = \frac{1}{2}\frac{g^2}{N^2}\overline{\left(\frac{T'}{\overline{T}}\right)^2}. \tag{3.13}$$

Here, overbars indicate temporal averages. According to linear theory, the energy per unit mass should grow exponentially with increasing height by a factor of $e^{z/H}$ (with H being the scale height) which is consistent with the exponential vertical decrease of air density and growth of GW amplitudes. In case of an increase of the vertical energy profiles smaller than $e^{z/H}$, an energy loss would be indicated, e. g., due to GW breaking. Furthermore, from linear GW theory, the ratio of kinetic to potential energy (E_{kin}/E_{pot}) is expected to have a nominal value of ∼5/3 (*VanZandt*, 1985). In summary, it can be stated that measurements of wind and temperature fluctuations in the mesosphere can be used to examine expectations from linear GW theory. This may be implemented by the combination of simultaneous measurements of horizontal radar winds and lidar temperatures which will be presented in the result section of this thesis (Chapter 5.3).

3.2 Gravity wave – mean flow interactions

After the short overview of linear GW theory and the demonstration of possibilities to test theoretical expectations with wind and temperature observations, the importance of GW as interacting features with the mean flow shall be highlighted. Most GW have small horizontal phase speeds in the order of the background mean flow. Thus they are very sensitive to critical level filtering by the background wind in the middle atmosphere such that their amplitudes depend on both the seasonal cycle as well as on planetary waves (e. g., *Manson et al.*, 2003; *Jacobi et al.*, 2006). After their generation mainly in the troposphere, GW propagate through the atmosphere and transport their energy and momentum from their source regions into higher atmospheric layers. Thereby, they can predominantly only reach higher altitudes when they move against the background wind. This means that under typical winter conditions with westerly winds at midlatitudes (positive wind speeds greater than ∼5 m/s), mainly GW with negative phase speeds or slight positive phase speeds of $c_{Ph} < 5$ m/s propagate up to upper mesospheric heights (Fig. 3.1, left). In contrast, GW with positive phase speeds in the order of the background wind are suppressed in the tropo- and stratosphere. This suppression of waves occurs due to critical level filtering, meaning that in case of the convergence of the wave phase speed c_{Ph} towards the mean zonal background flow $\overline{u}$, a critical level exists such that the GW are filtered by the mean wind and cannot pass through in vertical direction.

During summer (Fig. 3.1, right), the mean zonal wind is predominantly an easterly wind (with negative wind speeds), except for the tropo- and lower stratosphere where $\overline{u}$ is positive with values up to ∼20 m/s at midlatitudes. Then, only GW with positive phase speeds faster than this tropospheric and lower stratospheric flow can propagate upward, whereas GW with small positive phase speeds ($c_{Ph} < 20$ m/s) or negative phase speeds are suppressed. An additional exception of suppression are GW with very high positive phase speeds in winter or very high negative phase speeds in summer which are rare, but can also reach upper mesospheric heights nevertheless.

GW reaching the mesosphere grow exponentially in their amplitudes with increasing height due to the decreasing air density. This may consequently lead to instability of the GW and hence breaking. The breaking process starts just above stratopause heights in winter and in the upper mesosphere in summer. This height difference between winter and summer may be explained by the fact that the probability for the generation of GW with small phase speeds around zero (which can propagate upward in winter but are suppressed in summer) is greater than the generation of GW with higher phase speeds ($c_{Ph} > 20$ m/s)

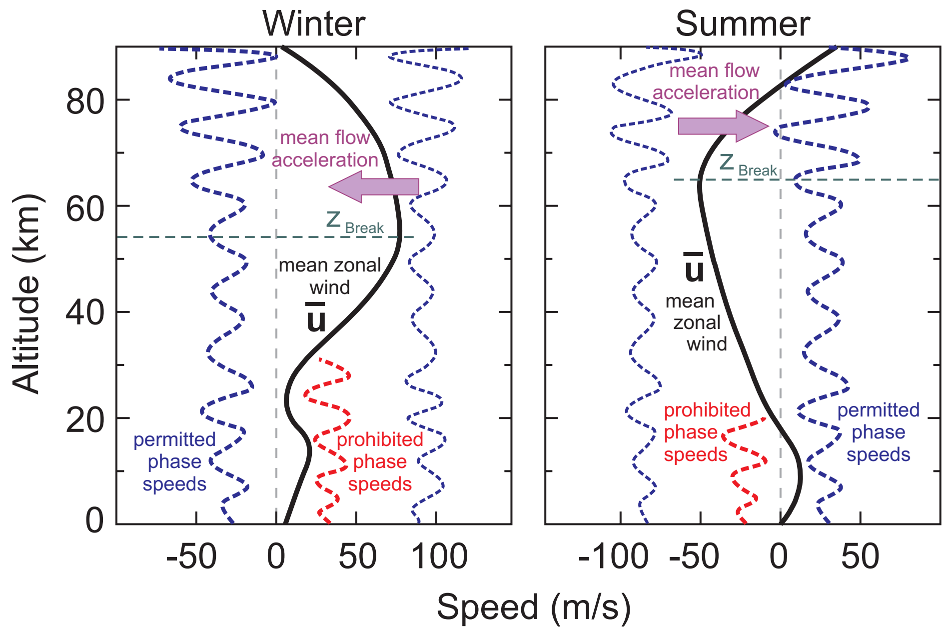

Figure 3.1: Schematic of typical vertical mean zonal wind profiles (black solid lines) for midlatitudes in winter (left) and summer (right) as well as indication of possible vertical GW propagation (dashed blue) and suppressed GW propagation (dashed red). The lower boundary of the GW breaking level is denoted by z_{Break}. Purple arrows indicate the direction of the mean flow acceleration due to GW breaking. See text for more information. This schematic is adopted from *Lindzen* (1981).

which are dominating in summer. This stronger influence of GW with low phase speeds in winter leads to a lower GW breaking level than in summer (*Lindzen*, 1981).

In the breaking process, the GW transfer their energy and momentum onto the background flow, thus inducing a force (the so-called "GW drag") which can accelerate or decelerate the mean flow. GW with negative phase speeds which dominate in winter cause a westward (negative) mean flow acceleration, whereas GW with positive phase speeds dominating in summer cause an eastward (positive) acceleration. As in summer the GW activity is most stable and dominated by high energetic short period GW, the mean flow acceleration is so strong that the whole wind regime can even be reversed. Hence, on the one hand the mean background wind influences the vertical propagation of GW by filtering them when reaching critical levels and on the other hand breaking GW modulate the upper mesospheric wind field. Consequently, as mentioned before in Chapter 1, GW drive the residual mesospheric circulation from the summer pole to the winter pole and cause the temperature minimum in the summer mesopause.

In general, the vertical flux of zonal ($u'w'$) and meridional ($v'w'$) momentum of GW balances the mesospheric momentum budget and their vertical divergence accelerates the mean flow. The mean momentum budget in the summer MLT is governed by the GW drag due to midfrequency GW and the Coriolis acceleration of the mean meridional wind ($f \cdot \overline{v}$). Here f is the Coriolis frequency and $\overline{v}$ is the mean meridional wind. The momentum balance in zonal direction is represented by the approximate equilibrium of the negative Coriolis acceleration and the GW drag which is represented by the density-weighted vertical divergence of the momentum flux:

$$-f \cdot \overline{v} \approx -\frac{1}{\overline{\rho}_0} \cdot \frac{\partial(\overline{\rho}\,\overline{u'w'})}{\partial z}\ . \qquad (3.14)$$

Here $\overline{\rho}$ is the mean density at particular heights above and below the reference height which has the mean reference density $\overline{\rho}_0$. The complete momentum budget must be formulated in the "transformed Eulerian-mean" (TEM) equations and includes the Stokes drift due to Rossby waves and inertia GW (cf. *Andrews et al.*, 1987). From Eq. 3.14 it becomes clear that a meridional flow which is turned into a zonal flow by the Coriolis force (due to the Earth's rotation) causes a change in the total angular momentum of the atmosphere which needs to be balanced by another source of momentum which is the momentum flux divergence. One main aim of this thesis is the investigation of these interactions between GW and the mean flow from observations at different locations by using different radar instruments and analysis methods (Chapters 5.1, 5.2, 5.4).

3.3 Atmospheric modeling with KMCM

The Kühlungsborn Mechanistic general Circulation Model (KMCM) is a primitive equation model (e. g., *Brasseur and Solomon*, 2005, their Chap. 3.9) which simulates the wind and temperature field in the atmosphere. It has been designed for investigating the global atmospheric dynamics with high spatial resolution. It explicitly resolves GW with periods of approximately 2–6 h and minimum horizontal wavelengths of 350 km, i. e., the resolution extends into the medium frequency part of the GW spectrum (*Becker*, 2009). Thus, the model yields a semi-realistic wave motion field. The KMCM is based on a standard spectral dynamical core (see *Simmons and Burridge* (1981) and references therein for description of the concept of spectral models and related numerical algorithms). The use of a triangular truncation at total wavenumber 120 (T120) determines the minimum resolved horizontal wavelength. In vertical direction, the model calculations are done on 190 hybrid levels from the surface to about 125 km height. This corresponds to a level spacing of approximately 600 m from the boundary layer to about 105 km height. The simulated GW scales are constrained by the spatial resolution. Simulations with increased resolution generally show GW with shorter horizontal wavelengths and somewhat higher frequencies (see *Becker*, 2009).

Wave dissipation is treated by an advanced turbulence parameterization. Also, waves interact non-linearly with the large-scale flow according to the non-acceleration theorem. As a result, the KMCM simulates a realistic GW drag and turbulent dissipation rate in the MLT. More details can be found in Paper II (Appendix C). A detailed description of the model concept is given in *Becker* (2009).

For the studies in this thesis, KMCM is used in a version without tidal waves. This is possible because the model is used with a simple radiation scheme in the form of a Newtonian temperature relaxation toward a constant radiative equilibrium background temperature (see *Becker*, 2009, and references therein). For further purposes an excitation of tides can simply be implemented (see *Becker*, 2011). In a latest work by *Knöpfel and Becker* (2011), a radiation scheme has been implemented allowing calculations of radiative flux densities and heating rates from the surface up to the lower thermosphere.

The simulations with the KMCM are mainly performed for permanent January conditions resulting in winter conditions for the northern hemisphere and summer conditions on the southern hemisphere. A corresponding model with an annual cycle has been applied in *Hoffmann et al.* (2010) in comparison with observations. The model output is on the model's hybrid surfaces for a latitude–longitude grid which can be chosen arbitrarily owing to the spectral transform method, i. e., data can be processed on a much smaller grid than that corresponding to the spectral resolution. In this thesis, wind and temperature fields as well as momentum fluxes are processed for comparative studies with measurements from radar and lidar instruments at certain geographical locations. As an example, Fig. 3.2 shows height-time cross-sections of zonal and meridional wind and temperature variations in the MLT region at the location of Kühlungsborn (54°N, 12°E) for an arbitrarily chosen 10-day time interval during winter. The variations are the deviations from the 10-day mean at each height. The model data is available with a snapshot interval of 11.25 min. The shown data is temporally

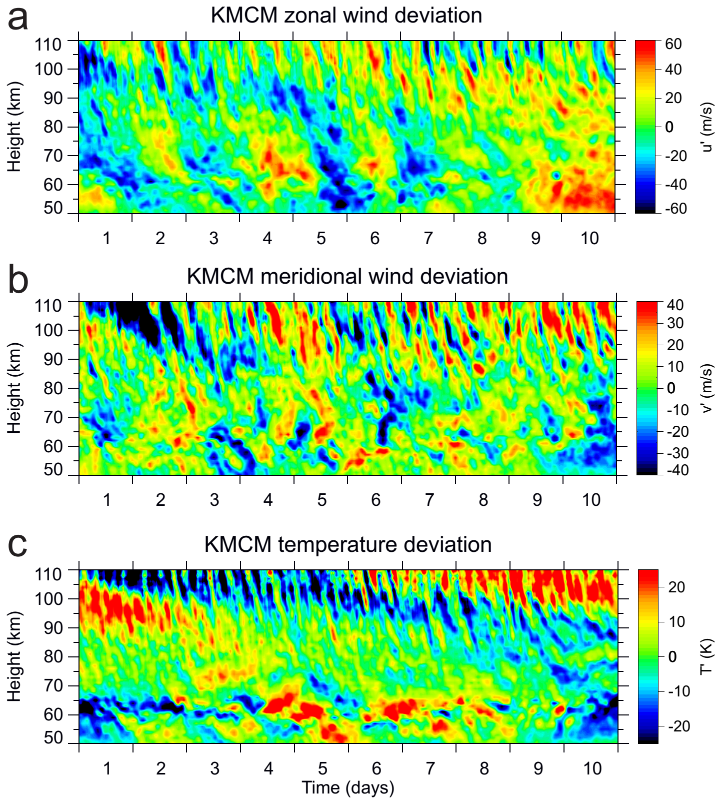

Figure 3.2: Height-time cross-sections of the zonal wind (a), meridional wind (b), and temperature (c) variations from the KMCM for the geographical position 54°N and 12°E. 10 consecutive model days under permanent January conditions are shown. The data has a time resolution of ∼30 min, integrated for ∼2 h. The height resolution is 1 km. This figure is taken from Paper III (Appendix C).

smoothed by a ∼2 h running mean, shifted by approximately half an hour. Furthermore, the model data is interpolated to a 1 km vertical resolution. The model wind and temperature variations reveal intensive wave structures with maximum amplitudes of 50 m/s (wind) and 25 K (temperature), respectively. The strongest wave-like events are visible in the mesopause region between about 85 and 100 km which is the height range where GW breaking mainly occurs. There, the wave phase lines have very steep vertical gradients whereas they are flatter at lower altitudes. Analogously, the vertical wavelength increases with height which mainly arises due to changes of the background wind which in turn cause changes of the intrinsic horizontal phase speeds (*Eckermann*, 1995). Also, the GW spectrum changes with increasing height due to critical level filtering.

Summarizing, Fig. 3.2 shows typical patterns of wind and temperature fluctuations in the northern winter MLT as simulated with the spectral general circulation model KMCM. The wind and temperature fields have comparable structures to observed fields from radars or lidars (see Paper III (Appendix C)). The simulated data may thus be used for comparisons with observations for understanding atmospheric processes. Furthermore, this GW-resolving model is ideal for defining, testing and optimizing GW analysis approaches and methods.

In this thesis the KMCM has been used for (a) validating a regression method by *Hocking* (2005) which determines wind variances and GW momentum fluxes from individual meteor observations in the mesopause (Chapter 5.2), (b) verifying predictions from the linear theory such as the polarization relations between wind and temperature variation and energy constraints (Chapter 5.3), as well as (c) comparing annual cycles of winds and momentum fluxes and checking the momentum balance in the MLT region in comparison with results from local observations (Chapter 5.4).

Chapter 4

Experimental Methods

4.1 Measurements with radar and lidar

Measurements of atmospheric GW are of great interest and importance in order to enlarge the knowledge and comprehension about the properties, occurrence and influences of GW in different atmospheric regions. For the studies in this thesis, radio waves measurements with radars (= **ra**dio **d**etection **a**nd **r**anging) and optical measurements with lidars (= **li**ght **d**etection **a**nd **r**anging) are used. Both kinds of measurement devices include instruments with excellent capabilities for monitoring the atmospheric dynamics. Thereby, radars are primarily specializing in temporally continuous wind observations in the tropo- and lower stratosphere as well as in the MLT region. Lidars measure temperature and can cover the whole altitude range from the ground up to the lower thermosphere, but often have temporally limited measurement periods as they are dependent on the prevailing weather conditions. The combination of radars and lidars allows advanced investigations of GW in the wind and temperature field. Observations from similar radars or lidars at different latitudes and longitudes give directly comparable information about the global distribution and properties of GW. Results of different types of radars or lidars which are possibly also retrieved from different analysis methods can be compared among each other and can be combined in height and time for enhanced investigations. Simultaneous observations of horizontal winds and temperatures also allow investigations of the polarization relations or kinetic and potential energy.

Atmospheric radar measurements base on the transmission of electromagnetic waves in the radio frequency range which are scattered or reflected at objects or certain targets. The transmitter antenna emits radio waves (the so-called radar signals) in predetermined directions which are then usually scattered or reflected at targets in many directions. The used radar signals usually lie in the MF (medium frequency) or VHF (very high frequency) range corresponding to wavelengths of 100–1000 m (MF) and 1–10 m (VHF). The received echo can be analyzed under certain criteria giving information about zenith angle and direction of the reflecting target, range (from the time shift between transmission and reception) and the relative movement (radial velocity) of the target with the wind field (relative to the stationary radar). The wind field is calculated from the Doppler effected frequency shift of the reflected signal. With this knowledge, the radial velocity can be converted to wind velocity in zonal, meridional and vertical direction (e. g., *Zecha*, 1999). The power of the echo signal gives information about the intensity (and consistence) of the reflecting targets in the observation area.

Scattering of radar waves takes place at inhomogeneities of the refractive index. In the tropo- and lower stratosphere, these inhomogeneities are variations of the water vapor content and temperature/density. In the mesosphere, these are changes in the electron density caused for example by turbulence or ambipolar diffusing meteors. A schematic of the radar principle and possible targets in the different atmospheric height regions is shown in Fig. 4.1 (left). The decisive advantage of radar wind observations is the independence from meteorological events

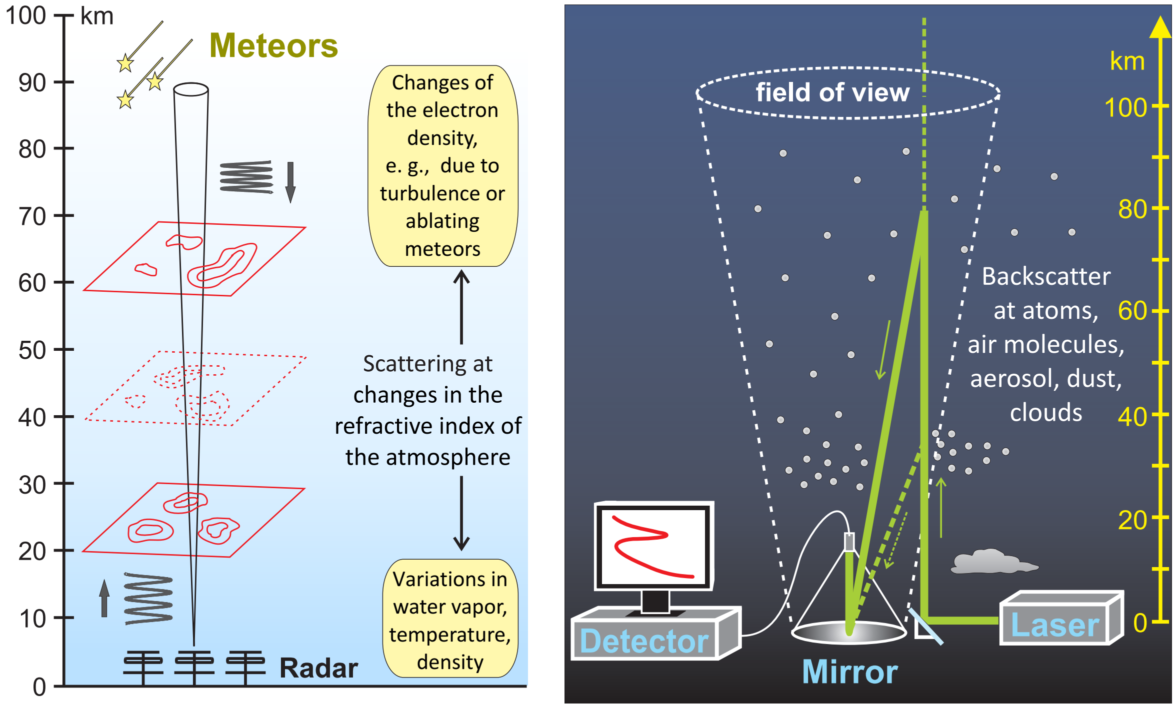

Figure 4.1: Schematics of radar (left) and lidar (right) measurements. See text for further information.

such that radars can do measurements continuously resulting in long consecutive time series for analyzing wave events. Also, the ability to monitor the mesosphere and mesopause region where GW amplification and breaking occurs is very important. However, a considerable drawback of radars is that there are no scattering or reflecting targets in the height range between about 20–60 km which limits the investigations of the vertical propagation of waves.

Atmospheric lidar measurements base on the transmission of pulsed laser light which is backscattered at atoms, molecules, and aerosol particles. The transmitted light lies in the ultraviolet (∼320–400 nm wavelength), visible (400–750 nm), or near infrared (750–1400 nm) range depending on the scope of application. The backscattered light is collected on a mirror system, gets through glass fibers and yields a signal at photon-counting detectors (Fig. 4.1, right). From the runtime of the signal and the speed of light, the distance (height) of the scattering targets can be determined thus yielding a vertical profile.

According to their application, different kinds of lidar are utilized making use of different types of backscattering. The most common types of backscattering are Rayleigh, Mie and Raman scattering as well as fluorescence at metallic atom layers of for instance sodium (Na), iron (Fe), or potassium (K). In case of Rayleigh scattering, the light is scattered elastically by particles much smaller than the wavelength of the light like, e. g., individual atoms or molecules. They absorb photons of the laser beam and re-emit photons with the same energy as the original photons. The analysis of the intensity of the backscattered light gives information about the air density and consequently, under the assumption of hydrostatic balance and by applying the ideal gas law, about the temperature. Mie scattering – or more general aerosol scattering – as a similar process, occurs at particles with sizes similar to the wavelength of light, i. e., aerosols, dust or cloud particles. While Rayleigh scattering depends strongly on the wavelength of the light, aerosol scattering has a less, but size-related wavelength dependence. Raman scattering is inelastic scattering of photons at atoms or molecules and can take place for any frequency of the incident light. It is connected with an excitation of the particles such that the scattered photons have a different (usually lower) frequency and energy than the incident photons. Resonance fluorescence is connected to a specific excitation frequency

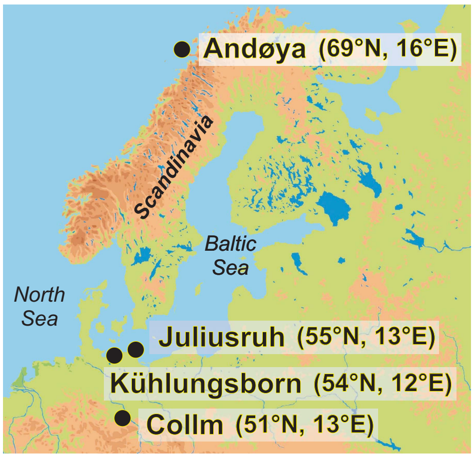

Figure 4.2: Geographical positions of the used radar and lidar instruments.

of the metal atoms. Metal lidars determine temperatures from the frequency shift due to the Doppler shift (broadening) of the backscattered resonance signal which depends on the temperature-associated movement of the particles. The combination of different lidar systems covering different altitude ranges allows a broad height coverage which is advantageous for monitoring the vertical GW propagation.

The used instruments for the measurements and analyses of this thesis are two MF radars at polar and midlatitudes, three SKiYMET meteor radars (one at polar and two at midlatitudes) and combined K-resonance and Rayleigh–Mie–Raman (RMR) lidar instruments at midlatitudes. The MF radars are located at Saura on the North-Norwegian island of Andøya (69°N, 16°E) and at Juliusruh on Rügen, Germany (55°N, 13°E). The SKiYMET meteor radar systems are located nearby Andenes on Andøya, at Juliusruh and at Collm Observatory nearby Leipzig, Germany (51°N, 13°E). The K and RMR lidar instruments are situated at Kühlungsborn, Germany (54°N, 12°E). Fig. 4.2 displays the geographical positions of these locations. All instruments are operated by the Leibniz Institute of Atmospheric Physics (IAP) at Kühlungsborn except for the meteor radar at Collm which is operated by the University of Leipzig.

MF radars are excellent instruments for the continuous observation of atmospheric dynamics like winds, tides, planetary waves, and internal GW. The here used MF radars at Saura and Juliusruh operate continuously since the years 2002 and 1990, respectively. They both use a Mills-Cross antenna consisting of 29 (Saura) and 13 (Juliusruh) crossed dipoles as schematically shown in Fig. 4.3 (left) for the Saura MF radar. Both MF radars have a very complex setup, but especially the very large-sized Saura MF radar is worldwide unique. Radio wave pulses of 2 km (Saura) and 4 km (Juliusruh) length are transmitted with a frequency of 3.17 MHz (Saura) and 3.18 MHz (Juliusruh), respectively. The peak pulse power is 116 kW (Saura) and 128 kW (Juliusruh). The received echo signals are sampled with a vertical resolution of 1 km (Saura) and 2 km (Juliusruh), respectively, for the investigations in this thesis. The height range covered by the two MF radars is 60–103 km (Saura) and 70–96 km (Juliusruh) whereby the lower limit for the latter can be extended down to 60 km for case studies. Mesospheric winds are analyzed with a temporal resolution of 4 min (Saura) and 30 min (Juliusruh). More detailed descriptions for the Saura MF radar can be found in *Singer et al.* (2008) and for the Juliusruh MF radar in *Keuer et al.* (2007).

Both MF radars can be operated in the Doppler beam steering (DBS) mode and the spaced antenna (SA) mode. In both cases all antennas forming the Mills-cross are used for transmission. When using the DBS mode, narrow radar beams are formed and transmitted in certain predefined directions and the whole transmitting antenna array is used for signal reception as well. When operating the MF radar in the SA mode, the radar signal is trans-

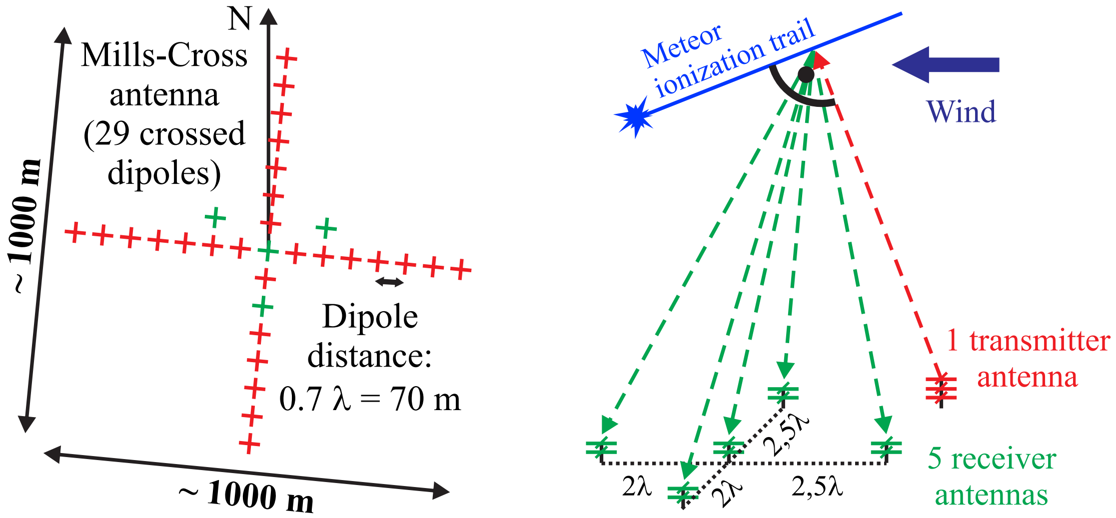

Figure 4.3: Schematics showing the setup of the antenna arrays of the Saura MF radar and a typical SKiYMET meteor radar. The parameter λ denotes the wavelength of the transmitted radar signal. See text for further information.

mitted only vertically and is received with individual antennas which are spatially separated from each other (indicated by green color in Fig. 4.3). The determination of the wind field from the Saura MF radar is realized by using the DBS mode and by making use of the Doppler effect which leads to a frequency shift of the reflected signal and yields the radial wind velocity. By combining several radial wind values from different beam tilt directions, the zonal, meridional, and vertical wind can be estimated. If the beams are tilted directly into zonal or meridional direction, the zonal and meridional wind can simply be calculated by trigonometry by taking the zenith angle into account. For the Juliusruh MF radar, the wind field is standardly determined by applying the full correlation analysis (FCA) method when operating the radar in the SA mode. From the cross correlation of the received signals at the spatially separated antennas, the horizontal wind field can be calculated. Additionally, this radar can also be run in the DBS mode yielding the three-dimensional wind field from the Doppler wind analysis. The latter has not been used in this thesis and is a matter of future studies.

The other type of radar used in this thesis are all-sky interferometric (SKiYMET) meteor radars. They are less extensive in dimensions, technique, and costs than MF radars, operate also continuous and automatic and allow a reasonable determination of winds as well. Owing to their minor complexity there exists a worldwide network of meteor radars with almost identical hard- and software which allow comparative studies for different locations, e. g., different latitudes. A fraction of this meteor radar network is presented in *Ward et al.* (2010) focussing on the equatorial region, but there exists a multitude of further meteor radars from low to polar latitudes around the globe.

Meteor radars use one transmitter antenna for emission of a circumpolar electromagnetic wave covering almost the whole sky and 5 receiver antennas which are arranged as an interferometer for signal reception (Fig. 4.3, right). The here used meteor radars at Andenes (Norway), Juliusruh and Collm (Germany) all have 3-element Yagi antennas except for the receiving antennas of the Collm meteor radar which are only 2-element Yagi antennas. Continuous observations are done since 2001 (Andenes), 2007 (Juliusruh), and 2004 (Collm). The signal transmission frequency is 32.55 MHz at Andenes and Juliusruh and 36.2 MHz at Collm. The peak powers are 18 kW at Andenes, 12 kW at Juliusruh, and 6 kW at Collm. Detailed information about these meteor radars can be found in *Singer et al.* (2004a) for Andenes, *Singer et al.* (2004b) for Juliusruh, and *Jacobi et al.* (2009) for Collm.

The transmitted signals are reflected at wind-drifted ionized ambipolar plasma trails from meteoroids entering the Earth's atmosphere and can be received (and interferometrically analyzed) if the trail is perpendicular to the connecting line between meteor radar and meteor trail. From the Doppler shift of the plasma trails, the radial drift velocity can be determined which is mainly caused by the neutral wind field at meteor ablation heights between about 80 and 100 km and thus also contains information of GW. The data analysis is performed within 6 height gates of 3 km vertical extent each (centered at 82, 85, 88, 91, 94, and 97 km) including sufficiently high count rates of reasonably uniformly distributed meteors for statistically reasonable results. As the meteor count rates are highest around ~ 90 km altitude (e. g., *Stober et al.*, 2008), data analysis can be performed with highest accuracy around this height whereas the decreasing number of meteors towards the lower and upper boundary can yield bigger measurement uncertainties. Winds are calculated on a temporal basis of 1 or 2 h by projecting the hourly or 2-hourly mean wind to each radial wind vector in that time interval and minimizing the squared differences according to the analysis method described by *Hocking et al.* (2001). An overview of the technical details of all used radar systems is arranged in Table A.1 (Appendix A).

The used K and RMR lidar instruments measure atmospheric temperatures at complementary altitudes. Based on the spectral Doppler broadening of the backscattered potassium D_1 resonance lines at 770 nm wavelength, the K lidar allows the determination of temperatures at metal layer altitudes between ~85 and 105 km. In the underlying heights down to the ground (~1–90 km), the RMR lidar measures the Rayleigh backscattering by air molecules and the spectral shape of the Rotational Raman spectrum with lasers at 532 and 355 nm wavelength. Detailed descriptions can be found in *Alpers et al.* (2004). From the Rayleigh backscattering, the air density can be determined and converted to temperature by hydrostatic integration. For this purpose the start temperature for the retrieval is taken from the K lidar at about 90 km height. Combined lidar measurements with the K and RMR system allow the worldwide unique possibility to measure vertical temperature profiles and temperature variations due to waves in the whole altitude range from 1 to 105 km. For the investigations in this thesis, temperature data with a temporal resolution of 30 min and a vertical resolution of 1 km is utilized. By using different radar and lidar instruments, GW can be studied from wind and temperature fluctuations over a broad height and time range. The main results of a study of combined radar and lidar measurements are summarized in Chapter 5.3.

4.2 Determination of gravity wave activity and momentum fluxes

For understanding the importance of GW and their influence on the dynamics of the middle atmosphere, GW activity and GW momentum fluxes are investigated from radar measurements in this thesis. The prior introduced SKiYMET meteor radars at polar and midlatitudes are ideal instruments for the determination of wind variances as a measure of GW activity and momentum fluxes describing the momentum transfer through the atmosphere. These parameters can be calculated simultaneously by applying a regression method from *Hocking* (2005) and can be compared for the different latitudes. The Saura MF radar is used for calculating momentum fluxes as well. These are derived from the classical dual-beam method from *Vincent and Reid* (1983). Both analysis methods will be scrutinized in the following.

The method from *Vincent and Reid* (1983) can be applied to DBS radars which transmit coplanar narrow radar beams in two opposite directions as schematically shown in Fig. 4.4 (left). The mean vertical flux of zonal momentum ($\overline{u'w'}$) and meridional momentum ($\overline{v'w'}$) can be estimated from tilted coplanar radar beams in zonal direction (West (W) and East

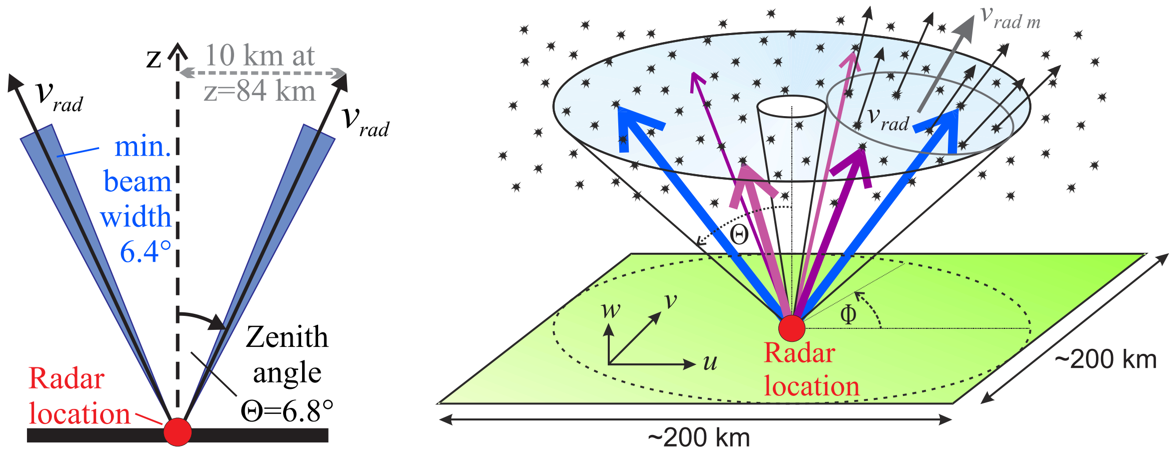

Figure 4.4: Schematics of the dual-beam method by *Vincent and Reid* (1983) (left) with typical properties of the Saura MF radar and the regression method by *Hocking* (2005) (right) applied to all-sky covering meteor radars. Colored arrows exemplary indicate opposite meteor positions. The radial wind velocity v_{rad} is estimated for each beam direction and meteor position, respectively. The mean v_{rad}-value under the assumption of a homogeneous background wind field (u, v, w) is indicated by $v_{rad\,m}$. Θ and Φ are the zenith and the azimuth angle, respectively.

(E)) and meridional direction (North (N) and South (S)):

$$u'w' = \frac{\overline{v'_{rad\,E}}^{2} - \overline{v'_{rad\,W}}^{2}}{2 \cdot \sin(2\Theta)} \,, \tag{4.1}$$

$$v'w' = \frac{\overline{v'_{rad\,N}}^{2} - \overline{v'_{rad\,S}}^{2}}{2 \cdot \sin(2\Theta)} \,. \tag{4.2}$$

Here, Θ denotes the zenith angle, overbars denote temporal averages, and v'_{rad} is the deviation of the measured radial wind velocity v_{rad} from the mean radial wind velocity in each tilt direction. Note, that here and in the following mean values of momentum fluxes as well as mean winds and mean wind variances are denoted without overbars for convenience.

The method from *Hocking* (2005) is a generalized dual-beam method that is fitted to meteor measurements which use an almost all-sky coverage as shown in Fig. 4.4 (right). For each individual meteor, the radial wind velocity is estimated such that principally many meteor pairs (exemplarily indicated by colored arrows in the schematic) could be investigated. Actually, with the method from *Hocking* (2005), mean momentum fluxes as well as mean wind variances are determined statistically by assuming that GW cause wind fluctuations which are seen in the deviations of individual radial wind values v_{rad} from the mean radial velocity $v_{rad\,m}$ expected for a uniform wind field. I. e., these deviations are determined as $v'_{rad} = v_{rad} - v_{rad\,m}$. From a least squares fit of these deviations, a matrix equation is obtained which may be solved for the mean wind variances in zonal (u'^2), meridional (v'^2), and vertical (w'^2) direction, the mean vertical flux of zonal momentum ($u'w'$) and of meridional momentum ($v'w'$) as well as the mean meridional flux of zonal momentum ($u'v'$). Detailed descriptions of this method can be found in *Hocking* (2005) as well as in Papers I and II (Appendix C). It must be noted that owing to the narrower observation area of the MF radar in contrast to the meteor radar, wave structures can be captured more precisely with the MF radar as they are averaged over a smaller spatial extent.

Furthermore, for the determination of statistically meaningful results from the different analysis methods, some selection criteria need to be applied to avoid outlier values being included in the calculations (e. g., *Murphy and Vincent*, 1993). Briefly, these outlier criteria concern radial wind values (v_{rad}) of the Saura MF radar and individual meteor events of the meteor radars. For instance, only v_{rad}-values being measured with a certain signal-to-noise ratio of the MF radar or lying within predefined magnitude limits are considered and signs of v_{rad}-values of opposite tilted MF radar beams are checked. For meteor radars, a minimum meteor number per height and time interval is required to guarantee a sufficient number of reasonably uniformly distributed meteors. Furthermore, certain limitations of the zenith angle from observed meteors and of the derived horizontal mean winds are declared. Detailed descriptions of the selection criteria can be found in the Papers I, II, and IV (Appendix C) for the corresponding MF and meteor radars and the respective application purposes.

Consequently, with the continuously operating MF and meteor radars, long-term observations of not only winds, but also GW activity and GW momentum fluxes are possible. Their seasonal variations can be investigated as well as their year-to-year variability. Meteor radars with almost identical hard- and software which operate at different locations like the here introduced instruments at polar (Andenes) and midlatitude sites (Juliusruh, Collm), allow latitudinal comparisons of GW activity and momentum fluxes. Momentum flux results of the different analysis methods for the different radar instruments (with narrow radar beams for MF radars and all-sky coverage for meteor radars) can be compared with each other. Moreover, coupling effects between mean background winds and GW can be investigated in detail as well as the derived momentum balance. These issues are in the focus of the present thesis whose results will be presented in the following Chapter.

Chapter 5

Results

5.1 Paper I (*Placke et al.*, 2011a): Gravity wave momentum fluxes in the MLT–Part I: Seasonal variation at Collm (51.3°N, 13.0°E)

This paper describes the extension of *Placke* (2008) and essentially is the first-time application of the relatively new method by *Hocking* (2005) to 5 years of observations with the all-sky interferometric (SKiYMET) meteor radar at Collm, Germany (51.3°N, 13.0°E). This analysis method allows the simultaneous determination of mean wind variances (u'^2, v'^2, w'^2) and momentum fluxes ($u'v'$, $u'w'$, $v'w'$) of short period GW in the upper mesosphere and lower thermosphere. Based on 5 years of observation (August 2004 through July 2009), the seasonal variation of wind variances as a measure of GW activity and GW-related momentum fluxes as well as their interannual variability has been studied at midlatitudes. Mean winds are analyzed on a 2-hourly basis according to the method described by *Hocking et al.* (2001). The meteor data analysis is carried out in height gates of 3 km vertical extent each in the height range between 83.5 and 95.5 km (nominal heights 85, 88, 91, and 94 km). Within these height gates a sufficient number of meteors is guaranteed for the applied least squares fit of all quantities. As in the lowermost and uppermost height gate covered by the meteor radar (nominal heights 82 and 97 km) the meteor count rates are too low at Collm due to technical reasons, no data analysis can be performed. To get significant results, the meteors used for the analysis have been restricted to zenith angles between 10 and 50° similar to the recommendations by *Hocking* (2005). Also, meteors with 2-hourly horizontal mean winds greater than 150 m/s are disregarded. The evaluation of the wind variances in zonal and meridional direction requires supplementary the consideration of artificially induced variance due to the background (prevailing or tidal) wind shear.

The main results of this study are the 5-year mean annual variation of the mean zonal wind (u), the mean zonal wind variance (u'^2) caused by short period GW and the mean GW momentum flux in zonal direction ($u'w'$) around mesopause heights at Collm (Fig. 5.1). Running averages over 28 days, shifted by 7 days, have been calculated and averaged over 5 years from August 2004 to July 2009. As the wind variance has a log-normal distribution, medians are used for averaging (see, e. g., *Baumgaertner and McDonald*, 2007). The Gaussian distributed mean wind and momentum flux are averaged by arithmetic means. Owing to the vertical distribution of meteors which maximize in number around 90 km, calculations are most accurate around this height.

In general, the mean zonal wind u has an annual variation at upper mesospheric heights with westward directed (negative) winds in the summer half-year and eastward directed (positive) winds in the winter half-year which can approximately be seen in the lower part of the considered altitude range in Fig. 5.1. Above about 88 km, a semi-annual wind pattern is present with eastward directed winds in summer and winter and westward directed winds

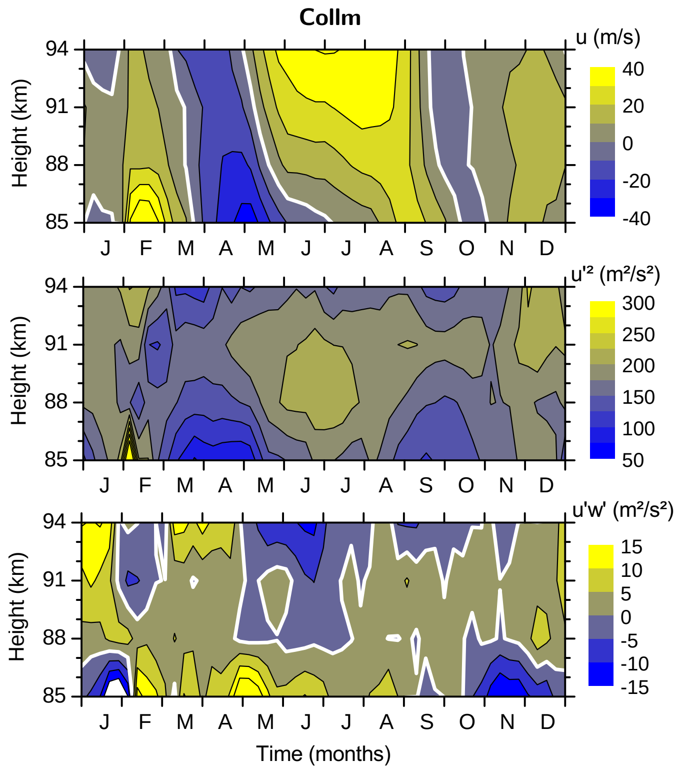

Figure 5.1: Height-time cross-sections for the mean zonal wind (upper panel), the wind shear corrected mean zonal wind variance (middle panel), and the mean vertical flux of zonal momentum (lower panel) from the meteor radar at the midlatitude site Collm. Running averages over 28 days, shifted by 7 days, have each been averaged within the period of five years (August 2004 - July 2009). This figure has been composed from Figs. 4 (partly) and 5 from Paper I (Appendix C).

around the equinoxes. The measured mean zonal wind has magnitudes of $\pm 40\,\mathrm{m/s}$. In March, the zonal wind reversal from winter to summer conditions occurs very abruptly over the whole considered height range whereas the summer zonal wind reversal takes place from May until July and slowly shifts down from 94 to 85 km.

The mean zonal wind variance u'^2 shows a semi-annual variation of the GW activity around 90 km and has magnitudes of approximately 100–$250\,\mathrm{m^2/s^2}$. The main maximum occurs in summer and a minor one in winter. The minima occur around the equinoxes with the spring minimum having slightly smaller values than the fall minimum. The position of the summer maximum (around 89 km) is somewhat lower than the winter maximum (around 93 km). This height difference may be due to the fact that the increasing eastward background wind above the summer zonal wind reversal damps upward propagating, eastward directed GW strongly in their amplitudes according to linear theory. In contrast, amplitudes of upward propagating and westward directed GW in winter can increase in the eastward directed background wind field over a higher altitude range according to the density decrease with height. The stronger u'^2-maximum in summer contrary to winter is consistent with a strong vertical background gradient of the zonal wind. The minima coincide with small vertical zonal wind shear and weak prevailing wind. Similar findings for midlatitudes have been presented by, e. g., *Gavrilov et al.* (2002) and *Jacobi et al.* (2006).

The vertical flux of zonal momentum $u'w'$ varies mainly between $\pm 5\,\mathrm{m^2/s^2}$ and is approximately anticorrelated to the mean zonal wind. I. e., vertical transport of eastward (westward) directed momentum corresponds to a westward (eastward) directed mean flow. This relationship clarifies that GW can only propagate upward when they move against the background wind field. Furthermore, the reversal of the summer zonal wind from a westward flow at the upper mesosphere to an eastward flow in the lower thermosphere can be explained by breaking GW which impose their momentum onto the background wind and induce a force onto the wind field at mesopause heights. I. e., below the summer zonal wind reversal, GW moving against the wind field (with positive $u'w'$) propagate upward, increase in their amplitudes, break, and cause the wind reversal. Consequently, above the breaking level (in the reversed lower thermosphere wind field) only a small fraction of GW with negative $u'w'$ remains which was strong enough to move with the background wind in the mesosphere. These connections between mean wind and GW momentum flux directly show the importance of GW in influencing the dynamics of the middle atmosphere and of the mean wind in filtering vertically propagating GW. Similar results giving insight into the coupling processes between GW and the background circulation arise from the meridional components of wind and momentum flux.

Finally, the interannual variability of 3-monthly means of zonal and meridional wind variance as well as of zonal wind has been investigated in this paper. Key results of these investigations are that in the summer months (June–August), means of all parameters have the highest values and are most stable from year to year. This can lead to the above-mentioned strong summer maximum of the GW activity. In winter (December–February), the interannual variability is strongest which may be explained by the influence of planetary waves on the middle atmosphere circulation. The wind variances and hence the GW activity have a slightly increasing tendency in the considered time period of 5 years, but this tendency is not significant so far.

In summary, the new regression method by *Hocking* (2005) has been applied to 5 years of observations (2004 through 2009) with the meteor radar at the midlatitude site Collm for the first time. Long-term mean monthly mean variances and momentum fluxes of GW with periods less than 2 h have been regarded in the upper mesosphere and lower thermosphere pointing out clearly the relationship between GW and mean horizontal background winds. In the following Chapter, in order to ensure the correctness of the applied method, a first-time evaluation will be performed by using model data. Furthermore, the utilization of the regression method will be extended to further meteor radars at mid- and also polar latitudes for latitudinal comparisons.

5.2 Paper II (*Placke et al.*, 2011b): Gravity wave momentum fluxes in the MLT–Part II: Meteor radar investigations at high and midlatitudes in comparison with modeling studies

After the first-time application of the regression method from *Hocking* (2005) to the 5-year dataset at the midlatitude site Collm (Chapter 5.1), this method will now be evaluated for the first time as part of a sensitivity study by using model data from the GW-resolving Kühlungsborn Mechanistic general Circulation Model (KMCM). MLT wind variances and GW momentum fluxes from meteor radars at the midlatitude site Juliusruh, Germany (54.6°N, 13.4°E), and the polar site Andenes, Norway (69.3°N, 16.0°E), have been derived in addition to the Collm meteor radar. This allows the examination of the relationship between GW and the horizontal mean flow for different locations and to perform a latitudinal comparison.

Besides Paper I, further applications of Hocking's method are published by, e. g., *Antonita et al.* (2008) or *Clemesha et al.* (2009). In the latter paper, the authors reported about numerical problems of Hocking's method in case of small vertical wind variances compared to the horizontal ones. In this respect, it is mandatory for additional applications to carry out a conceptual test of Hocking's method. This is presented in Paper II by use of the spatially high-resolution model KMCM. This spectral model provides wind data which include an explicit description of GW on a 3-dimensional grid in the Earth's atmosphere. Individual wind data within this grid can be seen as equivalents for meteor events as observed by meteor radars. For the conceptual test, data of 10 model days under permanent January conditions are regarded within an area of 2.5° × 2.5° around the geographical position of the polar reference location Andenes. 13×13 equally distributed model data points are considered as information given by meteors. They each have a certain zenith and azimuth angle relative to the central reference location at ground level. As for the meteor radar investigations, the zenith angle has been limited to 10–50° and evaluations have been performed within six height gates of 3 km vertical extent each (centered at 82, 85, 88, 91, 94, and 97 km). Further selection criteria are not required as there exist no outliers in the model data.

Estimates for the mean wind variances (u'^2, v'^2, w'^2) and momentum fluxes ($u'v'$, $u'w'$, $v'w'$) are determined on the one hand by applying the regression method from *Hocking* (2005) onto the model data and on the other hand by direct calculations from the model. For direct estimates, the fluctuating wind components (u', v', w') of each data point are calculated by subtracting the mean wind value of each investigated height gate from the instantaneous wind values. Mean second moments are then calculated by multiplying the fluctuation terms with each other and subsequent averaging. The averaging interval is chosen to be 4 h as the biggest fraction of GW activity arises from mid-frequency waves (periods of 2–6 h). Moreover, this interval is close to the one used for meteor radar investigations (2 h) and facilitates comparisons of model and observational results.

Initially, directly determined and from Hocking's method retrieved mean horizontal (u'^2, v'^2) and vertical (w'^2) wind variances are compared. The results of both calculations yield good agreements for u'^2- and v'^2-values in magnitudes and value distribution, but exhibit discrepancies for w'^2-values. The latter are very small (0–1 m^2/s^2) for the direct calculation from the vertical KMCM winds. In contrast, Hocking's method reveals w'^2-values which are 20 times larger and partly even negative (both for 4-hourly averages and averages over the whole 10-day case study). These negative values are mathematically possible solutions of Hocking's matrix equation, but are physically not correct. As the vertical winds simulated by the hydrostatic KMCM are small (about ±1 m/s) compared to the non-hydrostatic wind components detected by radar measurements in the mesosphere (about ±5 m/s), a sensitivity study has been carried out by artificially enhancing input model vertical winds by a factor of 5 and 10. This also yields a smaller ratio between horizontal and vertical wind fluctuations

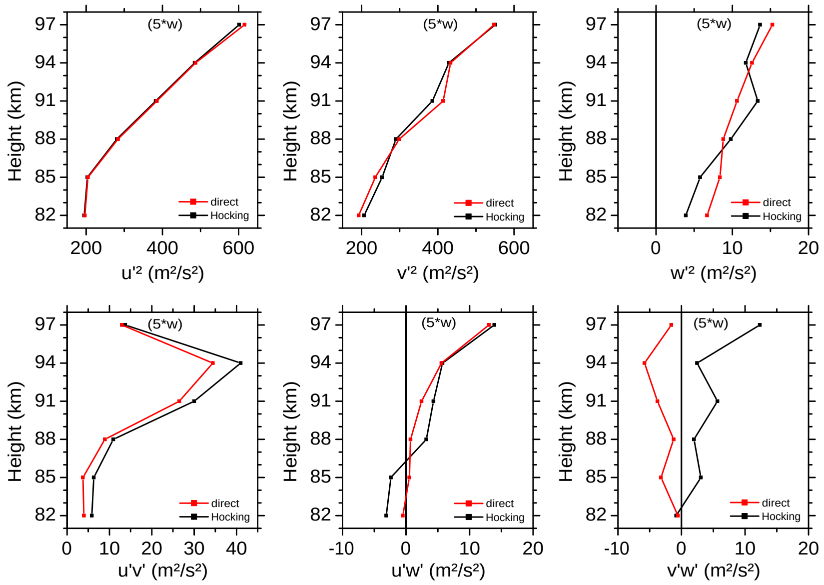

Figure 5.2: Mean vertical profiles of wind variances u'^2, v'^2, w'^2 (upper panels) and momentum fluxes $u'v'$, $u'w'$, $v'w'$ (lower panels) for the 5·w test-case. Averages for 10 model days in winter basing on 4-hourly data are shown. Red curves are directly determined values, black curves are results of Hocking's method. This figure is taken from Paper II (Appendix C).

which is typical for short period (and hence non-hydrostatic) GW. Note, that simulated horizontal winds have predominant magnitudes of –30 to 40 m/s which is similar to wind measurements by radars. With the amplified model vertical winds, the results for the wind variances and momentum fluxes of the direct calculations and from Hocking's method agree much better, especially the higher the factor for w is.

Fig. 5.2 shows the model mean vertical profiles of all considered parameters of 10 model days in winter for the calculations with w being multiplied by a factor of 5. This case compares best to wind magnitudes and the relation between horizontal and vertical wind variations obtained from radar measurements. Horizontal wind variances varying between 200 and 600 m^2/s^2 and the vertical wind variance having values of ∼4–15 m^2/s^2 are increasing with height. Their direct calculation and that by Hocking's method agree very well with the exception of some minor discrepancies for v' and some larger differences for w' compared to the magnitudes of the parameters. Also, the results for the meridional and the vertical flux of zonal momentum ($u'v'$ and $u'w'$) are in good agreement for both methods. Just the two profiles for the vertical flux of meridional momentum ($v'w'$) show more noticeable discrepancies for this 10-day model case study. In summary, this conceptual test confirms the applicability of the regression method by *Hocking* (2005) to wind data distributed over a reference location as in meteor radar measurements provided that input horizontal and vertical wind variations do not differ by more than a factor of about 3–5. Indeed, that is the case for real meteor radar observations.

In the following, Hocking's method is applied to the SKiYMET meteor radars at the midlatitude site Juliusruh and the polar site Andenes. The data analysis is carried out as in the previously presented paper (Chapter 5.1). The same height gates are used as well as the same meteor selection criteria and the correction for background wind shear that influences the horizontal wind variances. Figs. 5.3 and 5.4 show the results for the mean horizontal wind variances (u'^2, v'^2), the mean vertical flux of zonal momentum ($u'w'$) related to short period GW (periods ≤2 h) and the mean zonal wind (u) in the MLT region for both locations. The annual cycles have been constructed in the same way as the height-time cross-sections in Fig. 5.1 by calculating 28-day averages, shifted by 7 days. For this latitudinal comparison 2-year averages (July 2007 – June 2009) are shown. As introduced in Chapter 5.1, log-normal

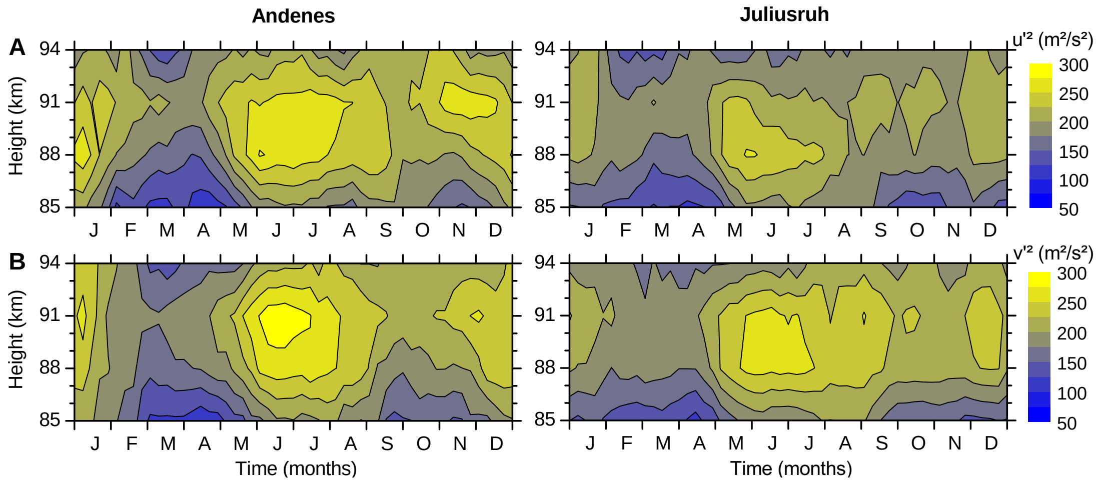

Figure 5.3: Height-time cross-sections of the mean zonal (A) and meridional (B) wind variance at the locations Andenes (left) and Juliusruh (right). Running averages over 28 days, shifted by 7 days, are shown, each averaged over two years (July 2007 – June 2009). This figure is adapted from Paper II (Appendix C) where more details are given.

distributed wind variances are averaged by using medians. For the Gaussian distributed mean winds and momentum fluxes, arithmetic means are calculated.

For both locations, Juliusruh and Andenes, the horizontal wind variances associated with GW activity show again a semi-annual variation in the MLT region with maxima in summer and winter and minima around the equinoxes. The main maximum in summer peaks at about $290\,\mathrm{m^2/s^2}$ (for v'^2) for Andenes and $\sim 270\,\mathrm{m^2/s^2}$ (also for v'^2) for Juliusruh each around 90 km. As at Collm, the secondary weaker winter maximum is located at slightly higher altitudes than the summer maximum. Possible reasons were discussed in Chapter 5.1. This height difference is stronger pronounced for the zonal wind variance u'^2 which has the winter maximum around 92 km. Further, the spring minimum with lowest values of $\sim 60\,\mathrm{m^2/s^2}$ at Andenes and $\sim 110\,\mathrm{m^2/s^2}$ at Juliusruh around 85 km for both u'^2 and v'^2 has slightly weaker values than the fall minimum. Altogether, the activity of short period GW at polar latitudes has more distinct magnitudes with stronger maxima and weaker minima than at midlatitudes.

Concerning the coupling between GW momentum fluxes and mean horizontal background winds, Fig. 5.4 shows the 2-year mean annual variation of the mean zonal wind u and zonal momentum flux $u'w'$ at the upper mesosphere and lower thermosphere region for Andenes and Juliusruh. Again, 28-day averages, shifted by 7 days, have been calculated for the observation period from July 2007 through June 2009. As mentioned for Collm, the zonal wind field of the upper mesosphere region is characterized by an annual cycle with westward directed (negative) winds in summer and eastward directed (positive) winds in winter up to ∼88 km. The lower thermosphere region (88–94 km) shows a more semi-annual variation with eastward directed winds in summer and winter and westward directed winds in spring and suggestively in fall (more distinct at Juliusruh than at Andenes). The zonal wind values lie between –30 and 40 m/s with positive winds being stronger pronounced at the midlatitude site Juliusruh than at polar latitudes. The change from winter to summer conditions in March occurs very abruptly over the whole considered height range. The zonal wind reversal during summer begins at 94 km height in May and shifts down to the upper mesosphere reaching 85 km in July (Juliusruh) and September (Andenes), respectively. Hence, at polar latitudes, the summer zonal wind reversal covers a longer time period and also takes place at higher altitudes than at midlatitudes. These differences occur due to the different breaking heights of the GW.

Considering again the annual cycle of the mean zonal wind together with the mean zonal momentum flux reveals that they are mainly directed opposite to each other, at least clearly during the summer half-year. The $u'w'$-values vary mainly between about $\pm 7\,\mathrm{m^2/s^2}$ at

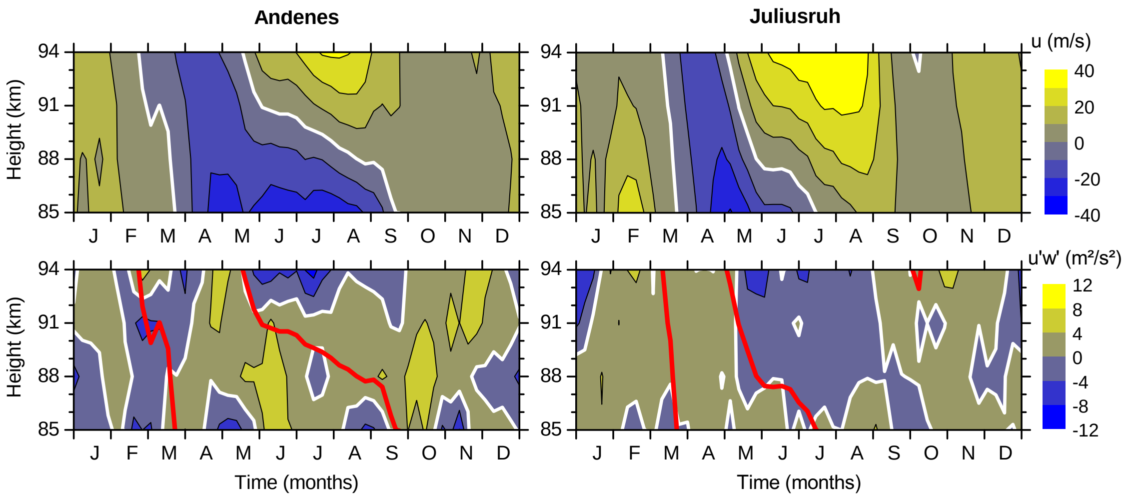

Figure 5.4: Height-time cross-sections of the mean zonal wind u (upper panels) and the mean vertical flux of zonal momentum $u'w'$ (lower panels) at the locations Andenes (left) and Juliusruh (right). Running averages over 28 days, shifted by 7 days, are shown, each averaged over two years from July 2007 through June 2009. Zero-lines of the displayed quantities are white. The red lines in the lower panels indicate the zero zonal wind line for each location. This figure is taken from Paper II (Appendix C).

Andenes and are a bit weaker at Juliusruh. As explained for Collm in Chapter 5.1, the correlation between GW and mean wind illustrates that GW can only propagate upward when they move against the prevailing mean flow because of critical level filtering. I. e., especially in the summer months when the activity of short period GW is strongest (see Fig. 5.3), eastward directed (positive) momentum fluxes coincide with westward directed (negative) winds and vice versa. This is a bit more distinctive at the midlatitude site Juliusruh than at the polar site Andenes. Additionally, the strong summer maximum of the variances coincides with the maximum vertical background wind gradient. The variance minima correspond to times with small vertical zonal wind shear and generally weak prevailing winds. Furthermore, the breaking of GW as a result of their amplification in the upper mesosphere due to the air density decrease with height is associated with the deposition of momentum onto the background flow. This leads to the mentioned summer zonal wind reversal around mesopause heights. The GW–mean flow coupling is especially obvious at Juliusruh as there the contrary sign reversals of u and $u'w'$ agree very well in summer. Positive summer mesospheric $u'w'$-values maximizing below the reversal height arise from the big fraction of GW moving against the background wind and causing the zonal wind reversal during their dissipation process. As these GW have then vanished, negative momentum flux values occur in the lower thermosphere due to a small fraction of strong GW which were able to move with the mesospheric background wind and can now enforce in the reversed wind field.

In conclusion, the regression method presented by *Hocking* (2005) has been validated for the first time by applying it to MLT model data from the GW-resolving general circulation model KMCM. The applicability of this method has been shown with the restriction that horizontal and vertical wind variations should not differ by more than a factor of about 3–5. In case of very small vertical winds compared to horizontal winds, terms containing w' show considerable discrepancies. Furthermore, the regression method has been applied to meteor radars at polar and midlatitudes showing direct connections between mean winds, wind variances, and GW momentum fluxes. Subsequently, the underlying linear theory of GW, especially the polarization relations between wind and temperature fluctuations, will be tested. For this purpose, both model data and wind and temperature observations from combined radar and lidar instruments will be investigated.

5.3 Paper III (*Placke et al.*, 2013): Testing linear gravity wave theory with simultaneous wind and temperature data from the mesosphere

In this paper, the underlying linear theory of GW in form of the polarization relations between wind and temperature fluctuations is scrutinized with respect to its applicability. The difficulty lies in the fact that, apparently, mesospheric observations often show a single dominant GW which could be considered for the validation of the linear wave theory. However, various waves – possibly interacting non-linearly with each other – are usually present at the same time but may not be obvious in the observations at first glance. Hence, the applicability of linear GW theory is far from obvious and shall be tested in this study. Therefore, a methodology is used in order to prove the fit of observational datasets to expectations from linear GW theory. Aspects of wavelet analysis, time series filtering, wave parameter analysis, polarization relations, as well as the determination of potential and kinetic energy will be considered for the MLT region. This methodology is initially checked with model data from KMCM and subsequently applied to simultaneous radar wind and lidar temperature measurements.

Horizontal winds and temperature from the KMCM form a suitable basis to test and optimize GW analysis methods for the verification of the predictions of the linear theory such as the polarization relations between GW-induced wind and temperature variation (T'/u' and T'/v'). 10 consecutive model days for permanent January conditions are arbitrarily chosen for the midlatitude position 54°N and 12°E. Around 92 km height, the strongest wave-like events occur (see also Fig. 3.2). Corresponding wavelet power spectra reveal dominant wave periods between 7 and 12 h for horizontal wind and temperature variations. Common Fourier power spectra of these parameters have similar dominant periods around 9–10 h. Filtering the time series at 92 km for the period band of strongest wave periods from the wavelet analysis (7–12 h) reveals that during the strongest wavelet power events, zonal and meridional wind variations are 90° phase-shifted. The same applies to the zonal wind and temperature variations. These findings are consistent with expectations from linear GW theory.

For a statistical validation of the polarization relations between wind and temperature variations, results for T'/u' and T'/v' are calculated from amplitudes of the filtered time series (u', v' and T') in the period band of 7–12 h and from wave parameters obtained from a Stokes parameters analysis (see Chapter 3.1). The Stokes parameters spectral analysis for the 10 model days is performed for 30-minute mean wind vertical profiles (wind variations after band pass filtering with the bandwidths of 7–12 h in time) following the procedure outlined in *Serafimovich et al.* (2005, 2006).

Fig. 5.5 shows the histograms for T'/u' and T'/v' for the whole 10-day case study of the KMCM in the height range from 80 to 99 km. This range covers the largest wave structures and is also the altitude range where radar and lidar observations have maximum amplitudes. The black histograms are calculated from the right hand sides of Eqs. 3.3 and 3.5. Estimates for the intrinsic frequency ω and the zonal, meridional and vertical wave numbers k, l and m are derived from the Stokes parameters analysis. The remaining parameters comprised in the equations (e. g., mean temperature, Coriolis frequency, etc.) are directly calculated from the model data for the considered height range and latitude, respectively. The red histograms are determined from the 12-h GW peak amplitudes, shifted by 30 min, of the filtered wind and temperature time series. I. e., these are the left hand sides of the same equations. The histograms of both calculations (from wave numbers and amplitude data) for T'/u' and T'/v', respectively, are in reasonable agreement. They show most frequent values between about 0.3 and 0.6 K/(m/s) derived from the wave numbers and a bit broader distributed values between 0.2 and 0.6 K/(m/s) derived from the amplitude data. The main peaks of the histograms from the wave numbers occur around 0.4–0.45 K/(m/s). The histograms from the 12-h peak

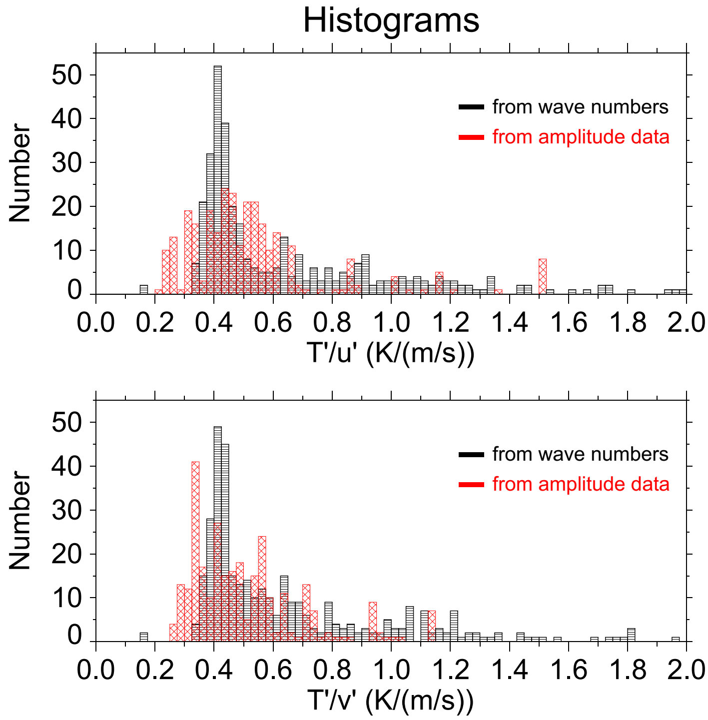

Figure 5.5: Histograms of the polarization relations T'/u' (upper panel) and T'/v' (lower panel) for the 10 KMCM model days. The black histograms show results calculated after Eqs. 3.3 and 3.5 containing the wave numbers which have been determined from Stokes parameters analysis. The red histograms are calculations of T'/u' and T'/v' from the 12-hour peak amplitudes of the filtered wind and temperature values. This figure is taken from Paper III (Appendix C).

amplitudes maximize at slightly higher values for T'/u' (0.45–0.5 K/(m/s)) and slightly lower values for T'/v' (around 0.35 K/(m/s)).

In an additional test, the KMCM kinetic and potential energy per unit mass are considered for the 10-day model case study between 80 and 96 km height. The potential energy per unit mass is derived by Eq. 3.13 by taking the temperature variations T' and the 10-day mean temperature per height $\overline{T}$ into account. The kinetic energy per unit mass (Eq. 3.12) is determined from the wind variations u' and v'. The results presented in Paper III show that a vertical energy increase up to about 86 km height is in accordance to the exponential amplitude growth ($e^{z/H}$) of GW due to the decreasing air density. Above that height, there is a weaker energy increase with height indicating an energy loss due to GW breaking. The ratio of kinetic and potential energy per unit mass also roughly follows expectations from linear GW theory by varying around a value of $\sim$5/3 (compare *VanZandt*, 1985). These findings support the approximate validity of linear GW theory for the KMCM data.

After this test with model data, the same methodology is applied to ground based mesospheric observations of simultaneous horizontal MF radar wind data at Juliusruh and temperature data from combined Potassium (K) and Rayleigh-Mie-Raman (RMR) lidars at Kühlungsborn. Both sites are almost located at the same latitude and have a horizontal distance of about 120 km. This is reasonably close for a comparative GW analysis with the different instruments provided that the horizontal wavelength of a considered wave is large compared to this distance. The first-time test of the linear GW theory with these radar and lidar instruments is based on continuous wind and temperature datasets from 11 to 13 October 2005 during the international CAWSES tidal campaign (for details see *Ward et al.*, 2010). This time period is characterized by very weak activity of tidal waves.

The horizontal wind and temperature variations for the 3-day case study are shown in

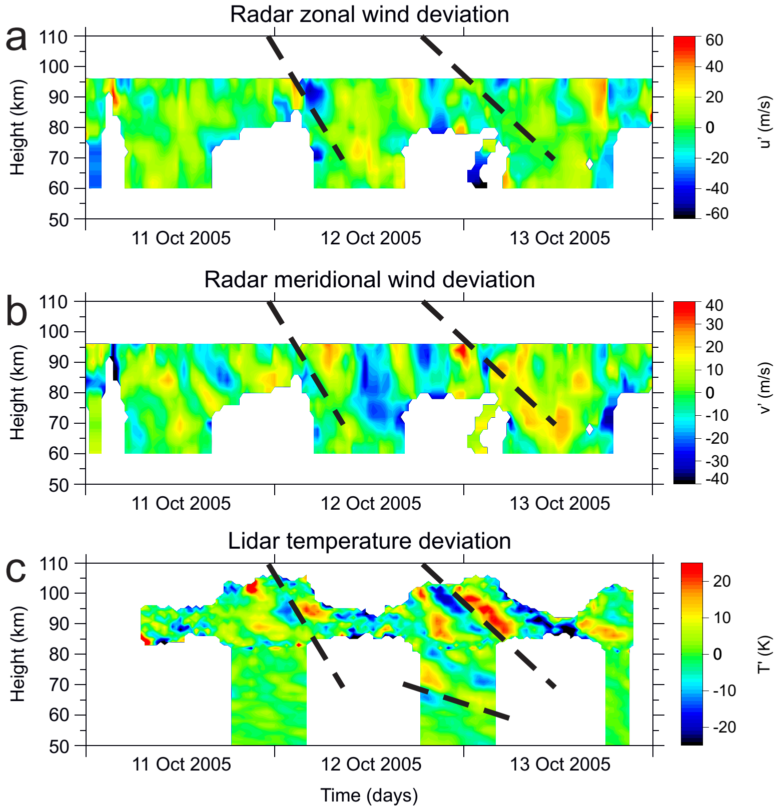

Figure 5.6: Height-time cross-sections of the zonal (a) and meridional (b) wind variations from the MF radar at Juliusruh and of the temperature variations (c) from the K and RMR lidar at Kühlungsborn. The data of both radar and lidar measurements has a time resolution of 30 min, integrated for 2 h. The height resolution of temperature and wind is 1 km and 2 km, respectively. Dashed lines show exemplary phase lines of waves occurring in all parameters at the same time. This figure is taken from Paper III (Appendix C).

Fig. 5.6 for the height range of 50–110 km. These variations are deviations from daily means which are calculated for a "lidar day", i. e., from noon of one day to noon of the subsequent day. The radar wind data is part of the long continuous time series of radar measurements with a broad daytime height coverage (∼60–96 km) due to high ionization rates in the mesosphere and narrower height coverage (∼80–96 km) during nighttime. The lidar temperature data covers almost three consecutive days in this case study and is a composite of K lidar data (∼85–105 km) and RMR lidar data (∼1–90 km). The lidar height coverage is temporal contrary to that of the radar, i. e., it is broadest during nighttime (∼18 LT – 04 LT) as the signal-to-noise ratio is highest in the darkness and narrowest during daytime when only the K lidar measures between ∼85 and 95 km. The wind and temperature variations lie mainly between ±30 m/s and ±25 K, respectively. The black dashed lines indicate exemplary phase lines of wave propagation in wind and temperature fields which steepen with increasing altitude due to the effect of the background wind.

From Fig. 5.6 it can also be seen that it is ambiguous to observe an obvious monochromatic GW which is evident over several cycles. Hence, suitable spectral analysis and band pass filtering is necessary to identify dominant wave components which can be traced over several cycles and checked for their agreement with linear GW theory. As for the model data, a wavelet analysis of the wind and temperature time series at 92 km is performed. At this height, radar and lidar measurements are continuous over the whole 3-day case study and have the largest wave amplitudes. Wavelet power spectra reveal dominant wave periods between 6 and 11 h especially around the transition from 12 to 13 October 2005. Fourier power spectra

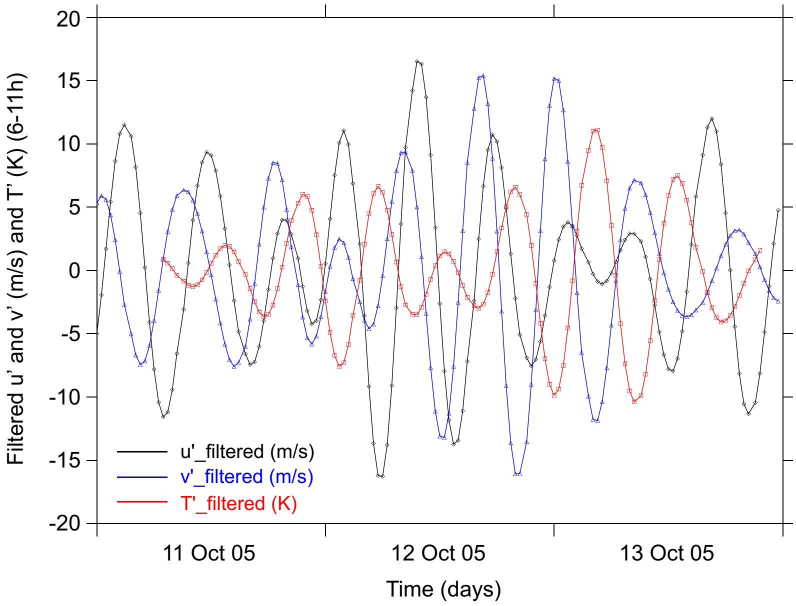

Figure 5.7: Filtered time series for 6 to 11 h for zonal wind variations u' (black line), meridional wind variations v' (blue line), and temperature variations T' (red line) at 92 km height for radar and lidar measurements. During the time with strongest amplitudes (12–13 October 2005) u' follows v' while v' is proportional to $-T'$. This figure is taken from Paper III (Appendix C).

of the horizontal wind and temperature variations have corresponding dominant peaks at 8 and 10 h. As the influence of tides is small during this case study, these variations are certainly caused by GW and not by tidal waves.

The wind and temperature time series at 92 km are filtered for the period band of strongest wave periods (6–11 h) from the wavelet analysis. Fig. 5.7 shows the filtered time series which reveal strongest amplitudes on 12 and beginning of 13 October. For this time period, zonal and meridional wind variations only have a small phase shift with u' following v'. Also, v' is anticorrelated with T', i. e., filtered meridional wind and temperature variations have a phase shift of 180°. These findings are consistent with the following results of a wave parameter analysis for the radar wind and lidar temperature data.

Additionally to the Stokes parameters analysis which had been applied to the KMCM model data, a hodograph analysis is initially performed to the radar and lidar measurements using the vertical profiles of the filtered values of u' and v' from Fig. 5.7 at the period with most intensive wave structures. From the hodograph analysis, the intrinsic period and zonal, meridional and vertical wave numbers are determined. Together with measurements of the remaining parameters (e. g., mean temperature, Coriolis frequency, etc.) on the right hand sides of Eqs. 3.3 and 3.5, the polarization relations are calculated. The results are $T'/u' = 0.23$ K/(m/s) and $T'/v' = 0.57$ K/(m/s), respectively, for 12 October 2005, 09:30 UT, between 76 and 94 km altitude. Furthermore, the hodograph for this time and height range reveals a GW propagation in approximately zonal direction.

While the hodograph analysis is based on the assumption of a dominating monochromatic GW at a particular time, the Stokes parameters analysis allows a statistical description of all present waves during the time period of strongest wave activity. Applying the Stokes parameters analysis to the time period of 12 October 2005, 06–18 UT, for 74–94 km height reveals again a zonal propagation direction of the GW. The mean phase difference between u' and v' is determined to $\sim$51.7° which is very close to the phase difference seen in Fig. 5.7 during the strongest wave activity. From the wave numbers estimated with the Stokes parameters analysis, the right hand sides of Eqs. 3.3 and 3.5 reveal $T'/u' = 0.14 \pm 0.01$ K/(m/s) and $T'/v' = 0.61 \pm 0.19\,\mathrm{K/(m/s)}$, respectively.

In summary, hodograph and Stokes parameters analysis result in similar intrinsic periods and propagation directions and almost identical zonal and vertical wave numbers. The meridional wave numbers have a stronger deviation which is mainly related to the dominating wave propagation in zonal direction. This is also roughly confirmed by the bigger standard deviation of T'/v' in contrast to the one of T'/u'.

Corresponding results for the polarization relations from the 12-h peak amplitudes of the filtered time series (Fig. 5.7), shifted by 30 min, for the same time (12 October 2005, 06–18 UT) but just at 92 km altitude, are calculated from the left hand sides of Eqs. 3.3 and 3.5. These results are $T'/u' = 0.41 \pm 0.11\,\mathrm{K/(m/s)}$ and $T'/v' = 0.46 \pm 0.12\,\mathrm{K/(m/s)}$. Both statistical methods (Stokes parameters analysis and mean 12-h peak amplitudes of the filtered time series) agree quite well, but slightly better for T'/v' than for T'/u'.

A final test of linear GW theory is performed by investigating the kinetic and potential energy per unit mass for the radar and lidar measurements in the MLT region. Similar to the results from the model dataset, 3-day mean vertical profiles of energy reveal increasing values in the height range from 80 to 96 km. Up to ∼86 km height, the gradients of the energy profiles follow approximately the $e^{z/H}$-line, i. e., GW amplitudes grow exponentially with height as expected from the linear theory. At the heights above, the increase of the vertical energy profiles is smaller than $e^{z/H}$ indicating an energy loss due to dissipation of GW. The ratio of kinetic to potential energy lies somewhat below the predicted value of 5/3, but is relatively constant over the whole considered height range. These moderate observed deviations from expectations of linear wave theory are possibly caused by a systematic underestimation of radar winds (and their variations), or by some violation of the linearity of the observed waves, i. e., different waves can be superposed or interact non-linearly which is not considered here.

Concluding the work of this paper, the application of the same methodology to KMCM model data and radar and lidar observations yields similarly conclusive results and hence gives evidence for the applicability of the linear GW theory to mesospheric observations after appropriate filtering of the considered time series. Finally, in the following last paper, the findings from Paper I and Paper II concerning the investigation of short period GW from meteor radar data by using Hocking's method will be evaluated with the powerful DBS capable Saura MF radar. This enables a clear validation of momentum flux results in the MLT region from two independently operating radar systems for which different analysis methods are used.

5.4 Paper IV (Unpublished manuscript): Mesospheric gravity wave momentum fluxes from radar measurements at polar latitudes in comparison with model results

The main issue of the last paper of this cumulative thesis is the evaluation of the relatively new method by *Hocking* (2005) for momentum flux determination from all-sky meteor radars versus the "classical" method introduced by *Vincent and Reid* (1983) for application to coplanar narrow-beam measurements of DBS capable MF radars. Two independently operating radar instruments at polar latitudes, the relatively simple SKiYMET meteor radar nearby Andenes and the co-located very complex MF radar at Saura, are taken into account. Having different designs and capabilities, these radars are used for the comparison of MLT winds and momentum fluxes from different operational modes and hence different applied analysis methods.

Initially, several selection criteria are chosen in order to avoid outlier values and to get statistically meaningful results from both radar instruments. For the Saura MF radar, the effect of different consecutively applied outlier criteria to radial wind velocity (v_{rad}-) values, which form the basis of the momentum flux calculations, is tested. The number of these v_{rad}-values included in the calculations per height gate is checked to be reasonable high enough. Also, the change of the vertical profiles of zonal ($u'w'$) and meridional ($v'w'$) momentum fluxes as part of the selection criteria is investigated. Overall, vertical momentum flux profiles between 70 and 100 km height have enhanced values of $u'w'$ above about 85 km and of $v'w'$ above about 93 km which is approximately the height range of GW breaking. For the Andenes meteor radar, the selection criteria concerning individual observed meteor events as introduced in the Papers I and II are applied.

Annual cycles of zonal and meridional winds and momentum fluxes in the years 2008, 2009 and 2010 as well as a 4-year mean annual cycle for 2008 through 2011 obtained with the two different analysis methods applied to the different radars are regarded. They reveal very similar patterns around mesopause heights compared to those presented in Paper I and II. Wind and momentum flux values from both methods show in general comparable annual variations and magnitudes, but they also present some differences between the applied dual-beam and the regression method.

The height-time cross-sections of the 4-year mean annual cycles of zonal wind and momentum flux from both radar instruments are shown in Fig. 5.8. The typical summer zonal wind reversal takes place at almost the same height (around 90 km) and time (May to September) for both instruments. Above that reversal, the meteor radar measures stronger zonal winds than the MF radar. Generally, the meridional winds are less pronounced than the zonal winds. Meridional winds measured with the meteor radar have stronger magnitudes over a longer time period in summer than the MF radar meridional winds. The momentum fluxes mainly amplify around mesopause heights which is more distinct in the results from the MF radar than from the meteor radar. This is also due to the narrower height range covered by the meteor radar and the lower meteor count rates in the lower- and uppermost height gates leading to more uncertainties of the calculated values. Hence, in contrast to the MF radar, the meteor radar gives only an approximate insight into the lower thermospheric wind and momentum flux fields.

Similar to the results presented in Paper I and II, the height-time cross-sections of MLT winds and momentum fluxes in both zonal and meridional direction are approximately anti-correlated clarifying the GW–mean flow interactions. Hence, vertical GW propagation is mainly only possible if GW move against the background wind. Also, the theory is confirmed that GW cause wind reversals around mesopause heights since above the region with strongest momentum deposition in summer the wind reverses. This is observable for both zonal (Fig. 5.8) and meridional components and is more distinct for the MF radar than

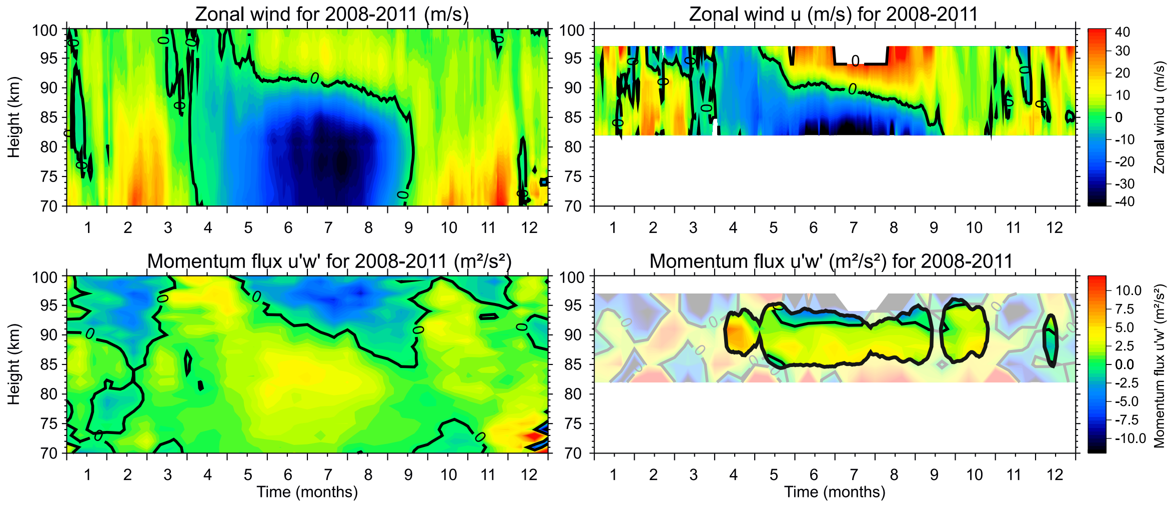

Figure 5.8: Height-time cross-sections of the 4-year mean annual cycles (2008 through 2011) of zonal wind (upper panels) and zonal momentum flux (lower panels) from the Saura MF radar (left) and the Andenes meteor radar (right). Mean winds are shown as running averages over 7 days, shifted by 1 day. Momentum fluxes are averages over 20 days, shifted by 10 days. The thick black contour lines within the $u'w'$-plot of the meteor radar denote significant regions with a sufficiently high meteor number per time and height interval. Not significant regions are shown with transparency. This figure is adapted from Paper IV (Appendix C) where more details are given.

for the meteor radar results. Stronger discrepancies occurring especially for the $v'w'$-values from the meteor radar may partly arise from inaccuracies in the calculations of the applied regression method in case of small vertical winds in comparison to the horizontal ones (compare Paper II).

Furthermore, there is a clear year-to-year variation of the zonal and meridional winds and momentum fluxes concerning the magnitudes, short-term fluctuations and also the temporal development of the zonal wind reversal. Such variations can for instance occur due to enhanced planetary wave activity in winter and are reflected in the results of both radar instruments. Summarizing, the use of the two independently operating radar instruments and the application of the different analysis techniques yields comparable results for horizontal winds and momentum fluxes in the MLT region. Thereby, the MF radar covers a broader height range than the meteor radar and reveals clearer structures of wind and momentum flux fields and their interactions.

For the correct interpretation of the determined results from the radar observations, model results from the KMCM have been considered as well. Annual cycles of zonally averaged horizontal winds and momentum fluxes at 69°N (corresponding to the MF and meteor radar location) are regarded covering a GW spectrum with wavelengths between 350 and 1000 km. In the investigated height range (70–100 km, as for the observations), the model zonal and meridional wind as well as the model vertical flux of zonal momentum have similar annual patterns with comparable magnitudes to the results from the radar measurements. The GW–mean flow interactions are very well reproduced in the zonal components of the KMCM, but are weaker pronounced in the meridional components.

Discrepancies between radar observations and model results appearing mainly in winter may be explained by the disturbing influence of stationary and transient planetary waves. Thus, in winter, the measurements at a certain location depend on the phase of the waves at this location possibly leading to deviating results from the model zonal-mean values. In summer, planetary waves are only weakly pronounced such that temporally averaged measurements are more representative for a zonal mean as presented by the KMCM. The

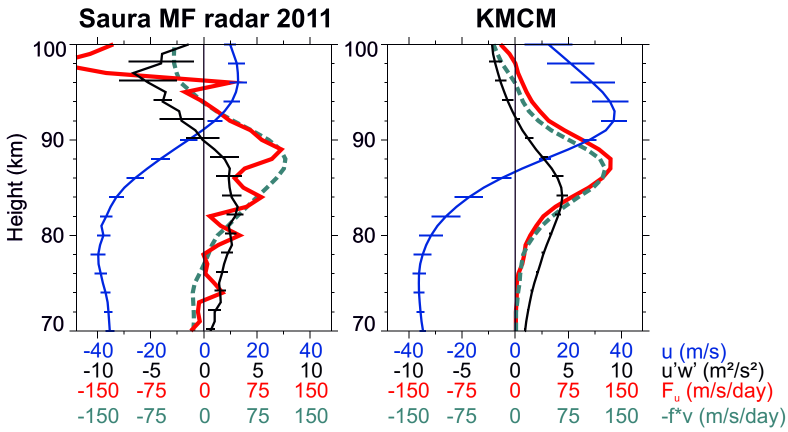

Figure 5.9: Monthly mean vertical profiles of zonal wind u (blue), momentum flux $u'w'$ (black) and GW drag F_u (red) as well as the negative Coriolis acceleration $-f \cdot v$ (green, dashed) for July from the Saura MF radar in 2011 (left) and the KMCM (right). Horizontal lines denote the standard deviation of wind and momentum flux at each height and are plotted only each 2 km for convenience. This figure is adapted from Paper IV (Appendix C).

weaker momentum flux values may be explained by the fact that this hydrostatic general circulation model simulates small vertical winds in contrast to non-hydrostatic mesospheric winds detected by radar instruments (compare Chapter 5.2 and Paper II (Appendix C)).

Finally, the mesospheric momentum balance is investigated for the Saura MF radar and KMCM model results. According to Eq. 3.14 (Chapter 3.2), it is expected that the GW drag approximately equals the negative Coriolis acceleration. Fig. 5.9 shows monthly mean vertical profiles of zonal wind, momentum flux and GW drag as well as the negative Coriolis acceleration from the radar observations in July 2011 and KMCM simulations for July. Focussing on summer gives a view on the balance during the time period with the strongest and most stable activity of short period GW, i. e., when the effect from disturbances like planetary waves is weakest. The vertical profiles of the zonal wind clearly show the strong mesospheric westward directed wind with maximum values of about –40 m/s around 80 km height and the eastward directed wind in the lower thermosphere. The latter is stronger pronounced in the model than in the radar measurements. The zonal wind reversal occurs at ∼90 km height for the radar and at ∼86 km for the model, respectively. For the MF radar, this height agrees excellent (for the KMCM approximately) with the reversal of the zonal momentum flux from positive values in the mesosphere to negative values in the lower thermosphere.

The vertical profiles of the GW drag and the negative Coriolis acceleration are in very good agreement for both MF radar measurements and model results. This means that, as a good approach, the momentum deposition balances the residual circulation due to the mean meridional wind. Also, the mean July vertical profiles of the meridional components of wind, momentum flux and GW drag have a distinct and clear structure although there are some discrepancies between radar and model results especially in the lower thermospheric values of the meridional momentum flux and GW drag.

Concluding this last paper, mesospheric horizontal winds and momentum fluxes have been determined from two different independently operating radar instruments at polar latitudes by applying different selection criteria and analysis methods. Annual cycles show a year-to-year variation of winds and momentum fluxes and clarify the GW–mean flow interaction. The findings from the radar measurements are completed and partly very well reproduced by model data from the GW-resolving KMCM. Furthermore, the summer mesospheric momentum balance has been confirmed from radar observations and model results.

Chapter 6

Conclusions and outlook

In this cumulative thesis, atmospheric gravity waves (GW) are investigated in the mesosphere and lower thermosphere region based on long-term radar observations. Measurements of winds, wind variances and GW momentum fluxes from different radar instruments at polar and midlatitudes using different analysis methods are utilized leading to a comprehensive understanding of GW and their effects on the background flow.

An analysis method proposed by *Hocking* (2005) for the simultaneous determination of wind variances caused by short period GW (period $\leq$2 h) and their related momentum fluxes is applied to all-sky interferometric meteor radars at the midlatitude sites Collm and Juliusruh and the polar site Andenes for the first time. Data analysis is carried out for periods of two and five years in consideration of certain selection criteria applied to the detected meteor events and of artificially induced variance due to the background wind shear.

Wind variances which are a measure of GW activity reveal a semi-annual variation around mesopause heights ($\sim$90 km) with a main maximum in summer occurring at somewhat lower altitudes than the minor winter maximum and with minima around the equinoxes. The stronger summer maximum is associated with the most stable GW activity which arises from the absence of disturbances like, e. g., planetary waves that dominate in winter and can filter GW. Furthermore, the summer maximum corresponds to the maximum vertical background wind gradient and the variance minima to times with small vertical zonal wind shear and generally weak prevailing winds. The activity of short period GW at polar latitudes has more distinct magnitudes with stronger maxima and weaker minima than at midlatitudes. Variances of the vertical wind are in general weak and show no significant annual variation at both latitudes.

Annual cycles of mean horizontal momentum fluxes and winds are approximately anti-correlated pointing out clearly the interactions between GW and the background mean flow. On the one hand, vertical GW propagation is controlled by the mean wind field which allows only vertical propagation of GW which move against the mean wind (i. e., momentum flux and wind have opposite sign). On the other hand, GW reaching the upper mesosphere amplify in their amplitudes due to the decreasing air density, may consequently break and deposit their momentum onto the background flow which can even lead to a reversal of the whole mesopause wind regime. This emphasizes the importance of GW in influencing the dynamics of the middle atmosphere. Such a wind reversal typically occurs in summer during strongest GW activity and has been observed to occur in polar regions at higher altitudes compared to midlatitudes.

Furthermore, the applicability of the analysis method by Hocking applied to the meteor radar data has been evaluated for the first time by use of the mechanistic general circulation model KMCM. This model provides a high spatial 3-dimensional resolution and an explicit description of GW. Mean wind variances and momentum fluxes have been determined directly from the fluctuating model wind components and from Hocking's method for 10 arbitrarily chosen model days. The conceptual test reveals that the mean vertical profiles of both calculations agree very well in the case of vertical wind variations differing less than a factor of 3–5 from the horizontal wind variations. Otherwise, results from Hocking's method have inaccuracies and give partly unphysical solutions.

The KMCM is also used for testing the applicability of the underlying linear theory of GW at midlatitudes. The polarization relations between horizontal wind and temperature fluctuations are validated statistically by estimating wave parameters from Stokes parameters analysis and by calculations from amplitudes of filtered wind and temperature time series. Vertical profiles of kinetic and potential energy per unit mass increase with height in accordance to the exponential amplitude growth of GW by $e^{z/H}$ below breaking level as expected from linear GW theory. Also, the ratio of kinetic to potential energy per unit mass roughly follows expectations from linear GW theory thus supporting the validity of this theory for mesospheric model data. Applying the same methodology to a 3-day case study of simultaneous horizontal MF radar wind at Juliusruh and combined K- and RMR-lidar temperature at Kühlungsborn (midlatitudes) yields similarly conclusive results for the polarization relations and vertical energy profiles. This gives evidence for the applicability of the linear GW theory to mesospheric observations after appropriate filtering of the time series.

Additionally, the mesospheric GW-related momentum fluxes obtained with the all-sky meteor radar at polar latitudes from the relatively new method by Hocking are evaluated with findings from co-located narrow-beam MF radar measurements using the "classical" dual-beam method from *Vincent and Reid* (1983). The meteor radar measurements are limited to meteor ablation heights (82–97 km) and give partly imprecise momentum flux results due to low meteor count rates especially in the winter months. In contrast, the MF radar has a broader height coverage (70–100 km) with longer-term more precise measurements owing to the narrower observation volume. The two independently operating radar instruments with the different applied analysis methods show similar annual patterns and magnitudes of winds and momentum fluxes around mesopause heights especially in the summer half-year. The advanced results from the MF Doppler radar give an improved insight into the coupling processes between GW and the background circulation with clearer characteristics in the zonal than in the meridional components. From three individual years (2008, 2009, 2010), a clear year-to-year variation is observed with the main differences occurring in the winter months due to the stronger disturbing influence from, e. g., planetary waves. 4-year mean annual cycles of horizontal winds and momentum fluxes from the radar measurements (2008 through 2011) correspond well to zonally averaged annual cycles from the KMCM at polar latitudes. An exception is the model meridional momentum flux which has a differing annual pattern and weaker magnitudes than the results from the radar measurements.

Finally, the mesospheric momentum balance in zonal direction is verified for the MF radar observations and KMCM model results at polar latitudes for summer when the activity of short period GW is most stable. Mean July vertical profiles of GW drag and Coriolis acceleration clearly and directly demonstrate that the GW momentum deposition into the wind field balances approximately the mean circulation.

In future studies, the investigations of winds, wind variances and GW momentum fluxes as performed for the polar latitude locations in Northern Norway and the midlatitude sites in Germany should be extended to further comparable instruments at more locations around the world. The application of Hocking's method to data of the world-wide network of meteor radars allows enhanced latitudinal and also longitudinal comparisons thus giving insight into the global structure of GW–mean flow interactions. In this context, further improvements of this regression method concerning, e. g., the filter criteria for individual meteors are necessary in order to raise the data quality and the temporal resolution. The investigation of the year-to-year variation of annual wind and momentum flux patterns from the independently operating MF and meteor radar at polar latitudes can be enhanced by focussing on the magnitudes, the temporal development and short-term variabilities of these parameters also in further years. Even though the year-to-year variability can be studied more clearly with the more complex MF radar, measurements from a network of meteor radars can support the investigation of long-term mean winds and momentum fluxes. Moreover, a spectral analysis of the horizontal momentum fluxes will give some indication of which part of the GW spectrum has the strongest contribution onto the total momentum flux. These investigations can additionally be performed for the similar MF and meteor radar located at the midlatitude site Juliusruh. This will allow a direct comparison of high-resolution narrow-beam MF radar momentum fluxes and will give insight into the year-to-year variation at different latitudes.

Furthermore, the test of linear GW theory which here has been carried out with simultaneous radar wind and lidar temperature measurements at midlatitudes can be extended for a longer case study possibly also at polar latitudes. Moreover, it is essential to conduct such investigations with observations in the same atmospheric volume with an identical spatial and temporal resolution. This could for instance be possible by using combined lidar instruments which measure both winds and temperature. Also, comparisons of local radar measurements with global satellite data are necessary and will broaden the knowledge about the world-wide distribution and properties of GW and their momentum fluxes.

Bibliography

Alexander, M. J. (1998), Interpretations of observed climatological patterns in stratospheric gravity wave variance, *J. Geophys. Res.*, *103*, 8627–8640, doi:10.1029/97JD03325.

Alexander, M. J., T. Tsuda, and R. A. Vincent (2002), Latitudinal variations observed in gravity waves with short vertical wavelengths, *J. Atmos. Sci.*, *59*, 1394–1404.

Allen, S. J., and R. A. Vincent (1995), Gravity wave activity in the lower atmosphere: Seasonal and latitudinal variations, *J. Geophys. Res.*, *100*(D1), 1327–1350, doi:10.1029/94JD02688.

Alpers, M., R. Eixmann, C. Fricke-Begemann, M. Gerding, and J. Höffner (2004), Temperature lidar measurements from 1 to 105 km altitude using resonance, Rayleigh, and rotational Raman scattering, *Atmos. Chem. Phys.*, *4*(3), 793–800.

Andrews, D. G., J. R. Holton, and C. B. Leovy (1987), *Middle atmosphere dynamics*, Academic Press, San Diego.

Antonita, T. M., G. Ramkumar, K. K. Kumar, and V. Deepa (2008), Meteor wind radar observations of gravity wave momentum fluxes and their forcing toward the Mesospheric Semiannual Oscillation, *J. Geophys. Res.*, *113*, D10115, doi:10.1029/2007JD009089.

Baumgaertner, A. J. G., and A. J. McDonald (2007), A gravity wave climatology for Antarctica compiled from Challenging Minisatellite Payload/Global Positioning System (CHAMP/GPS) radio occultations, *J. Geophys. Res.*, *112*, D05103, doi:10.1029/2006JD007504.

Baumgarten, G. (2010), Doppler Rayleigh/Mie/Raman lidar for wind and temperature measurements in the middle atmosphere up to 80 km, *Atmos. Meas. Tech.*, *3*, 1509–1518, doi:10.5194/amt-3-1509-2010.

Becker, E. (2009), Sensitivity of the Upper Mesosphere to the Lorenz Energy Cycle of the Troposphere, *J. Atmos. Sci.*, *66*, 647–666, doi:10.1175/2008JAS2735.1.

Becker, E. (2011), Dynamical Control of the Middle Atmosphere, *Space Sci. Rev.*, doi:10.1007/s11214-011-9841-5.

Beldon, C. L., and N. J. Mitchell (2009), Gravity waves in the mesopause region observed by meteor radar, 2: Climatologies of gravity waves in the Antarctic and Arctic, *J. Atmos. Solar Terr. Phys.*, *71*, 875–884, doi:10.1016/j.jastp.2009.03.009.

Brasseur, G. P., and S. Solomon (2005), *Aeronomy of the Middle Atmosphere: Chemistry and Physics of the Stratosphere and Mesosphere*, 3rd ed., Springer, Dordrecht, The Netherlands.

Briggs, B. H. (1984), The analysis of spaced sensor records by correlation techniques, in *Handbook for MAP*, vol. 13, edited by R. A. Vincent, pp. 166–186, SCOSTEP Secr., University of Illinois, Urbana.

Ceplecha, Z., J. Borovicka, W. G. Elford, D. O. Revelle, R. L. Hawkes, V. Porubcan, and M. Simek (1998), Meteor phenomena and bodies, *Space Sci. Rev.*, *84*, 327–471.

Clemesha, B. R., P. P. Batista, R. A. B. da Costa, and N. Schuch (2009), Seasonal variations in gravity wave activity at three locations in Brazil, *Ann. Geophys.*, *27*, 1059–1065.

Cot, C., and J. Barat (1986), Wave-turbulence interaction in the stratosphere: A case study, *J. Geophys. Res.*, *91*, 2749–2756.

Eckermann, S. D. (1995), Effect of background winds on vertical wavenumber spectra of atmospheric gravity waves, *J. Geophys. Res.*, *100*, 14,097–14,112.

Eckermann, S. D. (1996), Hodographic analysis of gravity waves: Relationships among Stokes parameters, rotary spectra and cross-spectral methods, *J. Geophys. Res.*, *101*(D14), 19,169–19,174.

Eckermann, S. D., and P. Preusse (1999), Global measurements of stratospheric mountain waves from space, *Science*, *286*, 1534–1537.

Eckermann, S. D., and R. Vincent (1989), Falling sphere observations gravity waves motions in the upper stratosphere over Australia, *Pageoph.*, *130*, 509–532.

Elford, W. G. (2001), Novel applications of MST radars in meteor studies, *J. Atmos. Solar Terr. Phys.*, *63*, 143–153.

Ern, M., P. Preusse, M. J. Alexander, and C. D. Warner (2004), Absolute values of gravity wave momentum flux derived from satellite data, *J. Geophys. Res.*, *109*(D20103), doi: 10.1029/2004JD004752.

Ern, M., P. Preusse, J. C. Gille, C. L. Hepplewhite, M. G. Mlynczak, J. M. R. III, and M. Riese (2011), Implications for atmospheric dynamics derived from global observations of gravity wave momentum flux in stratosphere and mesosphere, *J. Geophys. Res.*, *116*, D19107, doi:10.1029/2011JD015821.

Fleming, E. L., S. Chandra, J. J. Barnett, and M. Corney (1990), Zonal mean temperature, pressure, zonal wind, and geopotential height as functions of latitude, COSPAR international reference atmosphere: 1986, Part II: Middle atmosphere models, *Adv. Space Res.*, *10*(12), 11–59, doi:10.1016/0273-1177(90)90386-E.

Fritts, D. C., and M. J. Alexander (2003), Gravity wave dynamics and effects in the middle atmosphere, *Rev. Geophys.*, *41*(1), 3/1–64, doi:10.1029/2001RG000106.

Fritts, D. C., and D. Janches (2008), Dual-beam measurements of gravity waves over Arecibo: Reevaluation of wave structure, dynamics, and momentum fluxes, *J. Geophys. Res.*, *113*, D05112, doi:10.1029/2007JD008896.

Fritts, D. C., D. Janches, H. Iimura, W. K. Hocking, J. V. Bageston, and N. M. P. Leme (2012), Drake Antarctic Agile Meteor Radar first results: Configuration and comparison of mean and tidal wind and gravity wave momentum flux measurements with Southern Argentina Agile Meteor Radar, *J. Geophys. Res.*, *117*, D02105, doi:10.1029/2011JD016651.

Gavrilov, N. M., S. Fukao, T. Nakamura, C. Jacobi, D. Kürschner, A. H. Manson, and C. E. Meek (2002), Comparative study of interannual changes of the mean winds and gravity wave activity in the middle atmosphere over Japan, Central Europe and Canada, *J. Atmos. Solar Terr. Phys.*, *64*(8-11), 1003–1010, doi:10.1016/S1364-6826(02)00055-X.

Geller, M. A., and J. Gong (2010), Gravity wave kinetic, potential, and vertical fluctuation energies as indicators of different frequency gravity waves, *J. Geophys. Res.*, *115*, D11111, doi:10.1029/2009JD012266.

Gerding, M., J. Höffner, J. Lautenbach, M. Rauthe, and F.-J. Lübken (2008), Seasonal variation of nocturnal temperatures between 1 and 105 km altitude at 54°N observed by lidar, *Atmos. Chem. Phys.*, *8*, 7465–7482.

Gossard, E. E., and W. H. Hooke (1975), *Waves in the atmosphere, in Developments in Atmospheric Science*, vol. 2, Elsevier Sci., New York, 456 pp.

Hall, G. E., C. E. Meek, and A. H. Manson (1995), Hodograph analysis of mesopause region winds observed by three MF radars in the Canadian Prairies, *J. Geophys. Res.*, *100*(D4), 7411–7421.

Hecht, E. (2001), *Optik*, 3rd ed., Oldenbourg, München.

Hines, C. O. (1960), Internal atmospheric gravity waves at ionospheric heights, *Can. J. Phys.*, *38*(11), 1441–1481, doi:10.1139/p60-150.

Hocking, W. K. (2005), A new approach to momentum flux determinations using SKiYMET meteor radars, *Ann. Geophys.*, *23*(7), 2433–2439.

Hocking, W. K., B. Fuller, and B. Vandepeer (2001), Real-time determination of meteor-related parameters utilizing modern digital technology, *J. Atmos. Solar Terr. Phys.*, *63*(2-3), 155–169, doi:10.1016/S1364-6826(00)00138-3.

Hoffmann, P., W. Singer, and D. Keuer (2002), Variability of the mesospheric wind field at middle and Arctic latitudes in winter and its relation to stratospheric circulation disturbances, *J. Atmos. Solar Terr. Phys.*, *64*(8-11), 1229–1240, doi:10.1016/S1364-6826(02)00071-8.

Hoffmann, P., M. Rapp, J. Fiedler, and R. Latteck (2008), Influence of tides and gravity waves on layering processes in the polar summer mesopause region, *Ann. Geophys.*, *26*, 4013–4022.

Hoffmann, P., E. Becker, W. Singer, and M. Placke (2010), Seasonal variation of mesospheric waves at northern middle and high latitudes, *J. Atmos. Solar Terr. Phys.*, *72*, 1068–1079, doi:10.1016/j.jastp.2010.07.002.

Holton, J. R. (1982), The role of gravity wave induced drag and diffusion in the momentum budget of the mesosphere, *J. Atmos. Sci.*, *39*(4), 791–799, doi:10.1175/1520-0469(1982)039<0791:TROGWI>2.0.CO;2.

Holton, J. R., and M. J. Alexander (2000), The role of waves in the transport circulation of the middle atmosphere, in *Atmospheric Science Across the Stratopause*, *Geophys. Monogr. Ser.*, vol. 123, edited by D. E. Siskind, S. D. Eckermann, and M. E. Summers, pp. 21–35, AGU, Washington, D. C., doi:10.1029/GM123p0021.

Jacobi, C., N. M. Gavrilov, D. Kürschner, and K. Fröhlich (2006), Gravity wave climatology and trends in the mesosphere/lower thermosphere region deduced from low-frequency drift measurements 1984–2003 (52.1° N, 13.2° E), *J. Atmos. Solar Terr. Phys.*, *68*, 1913–1923, doi:10.1016/j.jastp.2005.12.007.

Jacobi, C., C. Arras, D. Kürschner, W. Singer, P. Hoffmann, and D. Keuer (2009), Comparison of mesopause region meteor radar winds, medium frequency radar winds and low frequency drifts over Germany, *Adv. Space Res.*, *43*, 247–252, doi:10.1016/j.asr.2008.05.009.

Keuer, D., P. Hoffmann, W. Singer, and J. Bremer (2007), Long-term variations of the mesospheric wind field at mid-latitudes, *Ann. Geophys.*, *25*(8), 1779–1790.

Knöpfel, R., and E. Becker (2011), An idealized radiative transfer scheme for use in a mechanistic general circulation model from the surface up to the mesopause region, *J. Quant. Spectrosc. Radiat. Transfer*, *112*, 1460–1478, doi:10.1016/j.jqsrt.2011.02.014.

Krebsbach, M., and P. Preusse (2007), Spectral analysis of gravity wave activity in SABER temperature data, *Geophys. Res. Lett.*, *34*(3), L03814, doi:10.1029/2006GL028040.

Lindzen, R. S. (1981), Turbulence and stress owing to gravity wave and tidal breakdown, *J. Geophys. Res.*, *86*, 9707–9714.

Lübken, F.-J. (1999), Thermal structure of the Arctic summer mesosphere, *J. Geophys. Res.*, *104*(D8), 9135–9149.

Lübken, F.-J., and U. von Zahn (1991), Thermal structure of the Mesopause Region at Polar Latitudes, *J. Geophys. Res.*, *96*(D11), 20,841–20,857.

Lue, H. Y., and F. S. Kuo (2012), Comparative studies of methods of obtaining AGW's propagation properties, *Ann. Geophys.*, *30*(3), 557–570, doi:10.5194/angeo-30-557-2012.

Manson, A., C. Meek, M. Hagan, C. Hall, W. Hocking, J. MacDougall, S. Franke, D. Riggin, D. Fritts, R. Vincent, and M. Burrage (1999), Seasonal variations of the semi-diurnal and diurnal tides in the mlt: multi-year MF radar observations from 2 to 70°N, and the GSWM tidal model, *J. Atmos. Solar Terr. Phys.*, *61*, 809–828.

Manson, A. H., C. E. Meek, and Q. Zhan (1997), Gravity wave spectra and direction statistics for the mesosphere as observed by MF radars in the Canadian Prairies (49°N–52°N) and at Tromsø (69°N), *J. Atmos. Solar Terr. Phys.*, *59*(9), 993–1009.

Manson, A. H., C. E. Meek, J. Koshyk, S. Franke, D. C. Fritts, D. Riggin, C. M. Hall, W. K. Hocking, J. MacDougall, K. Igarashi, and R. A. Vincent (2002), Gravity wave activity and dynamical effects in the middle atmosphere (60-90km): observations from an MF/MLT radar network, and results from the Canadian Middle Atmosphere Model (CMAM), *J. Atmos. Solar Terr. Phys.*, *64*, 65–90.

Manson, A. H., C. E. Meek, Y. Luo, W. K. Hocking, J. MacDougall, D. Riggin, D. C. Fritts, and R. A. Vincent (2003), Modulation of gravity waves by planetary waves (2 and 16 d): observations with the North American-Pacific MLT-MFR radar network, *J. Atmos. Solar Terr. Phys.*, *65*, 85–104.

Manson, A. H., C. E. Meek, C. M. Hall, S. Nozawa, N. J. Mitchell, D. Pancheva, W. Singer, and P. Hoffmann (2004), Mesopause dynamics from the scandinavian triangle of radars within the PSMOS-DATAR project, *Ann. Geophys.*, *22*(2), 367–386.

McLandress, C. (1998), On the importance of gravity waves in the middle atmosphere and their parameterization in general circulation models, *J. Atmos. Solar Terr. Phys.*, *60*, 1357–1383.

Mitchell, N. J., and C. L. Beldon (2009), Gravity waves in the mesopause region observed by meteor radar: 1. A simple measurement technique, *J. Atmos. Solar Terr. Phys.*, *71*(8-9), 866–874.

Muraoka, Y., S. Fukao, T. Sugiyama, M. Yamamoto, T. Nakamura, T. Tsuda, and S. Kato (1994), Features of a mesospheric inertio-gravity wave observed with the MU radar, *J. Atmos. Terr. Phys.*, *56*(9), 1163–1171.

Murphy, D. J., and R. A. Vincent (1993), Estimates of momentum flux in the mesosphere and lower thermosphere over Adelaide, Australia, from March 1985 to February 1986, *J. Geophys. Res.*, *98*(D10), 18,617–18,638, doi:10.1029/93JD01861.

Placke, M. (2008), Analyse kurzperiodischer Windschwankungen im Mesopausenbereich, Diploma thesis, Universität Leipzig.

Placke, M., G. Stober, and C. Jacobi (2011a), Gravity wave momentum fluxes in the MLT–Part I: Seasonal variation at Collm (51.3° N, 13.0° E), *J. Atmos. Solar Terr. Phys.*, *73*, 904–910, doi:10.1016/j.jastp.2010.07.012.

Placke, M., P. Hoffmann, E. Becker, C. Jacobi, W. Singer, and M. Rapp (2011b), Gravity wave momentum fluxes in the MLT–Part II: Meteor radar investigations at high and mid-latitudes in comparison with modeling studies, *J. Atmos. Solar Terr. Phys.*, *73*, 911–920, doi:10.1016/j.jastp.2010.05.007.

Placke, M., P. Hoffmann, M. Gerding, E. Becker, and M. Rapp (2013), Testing linear gravity wave theory with simultaneous wind and temperature data from the mesosphere, *J. Atmos. Solar Terr. Phys.*, *93*, 57–69, doi:10.1016/j.jastp.2012.11.012.

Preusse, P., M. Ern, S. D. Eckermann, C. D. Warner, R. H. Picard, P. Knieling, M. Krebsbach, J. M. Russell III, M. G. Mlynczak, C. J. Mertens, and M. Riese (2006), Tropopause to mesopause gravity waves in August: Measurement and modeling, *J. Atmos. Solar Terr. Phys.*, *68*, 1730–1751, doi:10.1016/j.jastp.2005.10.019.

Rapp, M., B. Strelnikov, A. Müllemann, F.-J. Lübken, and D. C. Fritts (2004), Turbulence measurements and implications for gravity wave dissipation during the MaCWAVE/MIDAS rocket program, *Geophys. Res. Lett.*, *31*(L24S07), doi:10.1029/2003GL019325.

Rauthe, M., M. Gerding, J. Höffner, and F.-J. Lübken (2006), Lidar temperature measurements of gravity waves over Kühlungsborn (54°N) from 1 to 105 km: A winter-summer comparison, *J. Geophys. Res.*, *111*(D24), D24108, doi:10.1029/2006JD007354.

Rauthe, M., M. Gerding, and F.-J. Lübken (2008), Seasonal changes in gravity wave activity measured by lidars at mid-latitudes, *Atmos. Chem. Phys. Discuss.*, *8*, 13,741–13,773.

Reid, I. M., and R. A. Vincent (1987), Measurements of mesospheric gravity wave momentum fluxes and mean flow accelerations at Adelaide, Australia, *J. Atmos. Terr. Phys.*, *49*(5), 443–460.

Riggin, D. M., C. K. Meyer, D. C. Fritts, M. J. Jarvis, Y. Murayama, W. Singer, R. A. Vincent, and D. J. Murphy (2003), MF radar observations of seasonal variability of semidiurnal motions in the mesosphere at high northern and southern latitudes, *J. Atmos. Solar Terr. Phys.*, *65*, 483–493.

Schmidt, T., A. de la Torre, and J. Wickert (2008), Global gravity wave activity in the tropopause region from CHAMP radio occultation data, *Geophys. Res. Lett.*, *35*, L16807, doi:10.1029/2008GL034986.

Serafimovich, A., P. Hoffmann, D. Peters, and V. Lehmann (2005), Investigation of inertia-gravity waves in the upper troposphere / lower stratosphere over Northern Germany observed with collocated VHF/UHF radars, *Atmos. Chem. Phys.*, *5*, 295–310.

Serafimovich, A., C. Zülicke, P. Hoffmann, D. Peters, P. Dalin, and W. Singer (2006), Inertia Gravity Waves in the Upper Troposphere during the MaCWAVE Winter Campaign, Part II: Radar investigations and modelling studies, *Ann. Geophys.*, *24*, 2863–2875.

Simmons, A. J., and D. M. Burridge (1981), An energy and angular-momentum conserving vertical finite-difference scheme and hybrid vertical coordinates, *Mon. Wea. Rev.*, *109*, 758–766.

Singer, W., U. von Zahn, and J. Weiß (2004a), Diurnal and annual variations of meteor rates at the arctic circle, *Atmos. Chem. Phys.*, *4*, 1355–1363.

Singer, W., J. Bremer, J. Weiß, W. K. Hocking, J. Höffner, M. Donner, and P. Espy (2004b), Meteor radar observations at middle and arctic latitudes – Part 1: Mean temperatures, *J. Atmos. Solar Terr. Phys.*, *66*, 607–616, doi:10.1016/j.jastp.2004.01.012.

Singer, W., R. Latteck, and D. A. Holdsworth (2008), A new narrow beam Doppler radar at 3 MHz for studies of the high-latitude middle atmosphere, *Adv. Space Res.*, *41*(5), 1488–1494, doi:10.1016/j.asr.2007.10.006.

Stober, G., C. Jacobi, K. Fröhlich, and J. Oberheide (2008), Meteor radar temperatures over Collm (51.3°N, 13°E), *Adv. Space Res.*, *42*, 1253–1258, doi:10.1016/j.asr.2007.10.018.

Suzuki, S., T. Nakamura, M. K. Ejiri, M. Tsutsumi, K. Shiokawa, and T. D. Kawahara (2010), Simultaneous airglow, lidar, and radar measurements of mesospheric gravity waves over Japan, *J. Geophys. Res.*, *115*, D24113, doi:10.1029/2010JD014674.

Tsuda, T., M. Yamamoto, T. Sato, S. Kato, and S. Fukao (1985), Comparison observations between the MU radar and the Kyoto meteor radar, *Radio Sci.*, *20*(6), 1241–1246, doi:10.1029/RS020i006p01241.

VanZandt, T. E. (1985), A model for gravity wave spectra observed by Doppler sounding systems, *Radio Sci.*, *20*(6), 1323–1330.

Vincent, R. A., and D. C. Fritts (1987), A climatology of gravity wave motions in the mesopause region at Adelaide, Australia, *J. Atmos. Sci.*, *44*(4), 748–760, doi:10.1175/1520-0469(1987)044<0748:ACOGWM>2.0.CO;2.

Vincent, R. A., and I. M. Reid (1983), HF Doppler measurements of mesospheric gravity wave momentum fluxes, *J. Atmos. Sci.*, *40*(5), 1321–1333.

von Zahn, U., and W. Meyer (1989), Mesopause Temperatures in Polar Summer, *J. Geophys. Res.*, *94*(D12), 14,647–14,651, doi:10.1029/JD094iD12p14647.

Ward, W. E., J. Oberheide, L. P. Goncharenko, T. Nakamura, P. Hoffmann, W. Singer, L. C. Chang, J. Du, D.-Y. Wang, P. Batista, B. Clemesha, A. H. Manson, D. M. Riggin, C.-Y. She, T. Tsuda, and T. Yuan (2010), On the consistency of model, ground-based, and satellite observations of tidal signatures: Initial results from the CAWSES tidal campaigns, *J. Geophys. Res.*, *115*, D07107, doi:10.1029/2009JD012593.

Woodman, R. F., and A. Guillen (1974), Radar observations of winds and turbulence in the stratosphere and mesosphere, *J. Atmos. Sci.*, *31*, 493–505.

Wright, C. J., and J. C. Gille (2011), HIRDLS observations of gravity wave momentum fluxes over the monsoon regions, *J. Geophys. Res.*, *116*, D12103, doi:10.1029/2011JD015725.

Wüst, S., and M. Bittner (2006), Non-linear resonant wave-wave interaction (triad): Case studies based on rocket data and first application to satellite data, *J. Atmos. Solar Terr. Phys.*, *68*(9), 959–976, doi:10.1016/j.jastp.2005.11.011.

Zecha, M. (1999), Untersuchung der polaren sommerlichen Mesosphäre mit unterschiedlichen Radarverfahren im VHF-Bereich, Ph.D. thesis, Universität Rostock.

Zink, F. (2000), Gravity waves and turbulence in the lower atmosphere, Ph.D. thesis, University of Adelaide, Australia.

Appendix A

Table

Table A.1: Technical details of the used radar systems

Radar type	MF		Meteor (VHF)		
Location	Saura (69°N, 16°E)	Juliusruh (55°N, 13°E)	Andenes (69°N, 16°E)	Juliusruh (55°N, 13°E)	Collm (51°N, 13°E)
Frequency	3.17 MHz	3.18 MHz	32.55 MHz	32.55 MHz	36.2 MHz
Peak power	116 kW	128 kW	18 kW	12 kW	6 kW
Height range	60–103 km	70–96 km	80–100 km	80–100 km	80–100 km
Sampling res.	1 km	2 km	3 km	3 km	3 km
Wind analys.	DBS	FCA, DBS	Doppler	Doppler	Doppler
Time res.	4 min	30 min	2 h	2 h	2 h
Observations since	2002	1990	2001	2007	2004

Appendix B

List of included publications and manuscripts

This thesis summarizes the following publications and manuscripts:

- Paper I (Appendix C: page 51)
  Placke, M., G. Stober, and C. Jacobi (2011a), Gravity wave momentum fluxes in the MLT–Part I: Seasonal variation at Collm (51.3° N, 13.0° E), *J. Atmos. Solar Terr. Phys.*, *73*, 904–910, doi:10.1016/j.jastp.2010.07.012.

- Paper II (Appendix C: page 59)
  Placke, M., P. Hoffmann, E. Becker, C. Jacobi, W. Singer, and M. Rapp (2011b), Gravity wave momentum fluxes in the MLT–Part II: Meteor radar investigations at high and midlatitudes in comparison with modeling studies, *J. Atmos. Solar Terr. Phys.*, *73*, 911–920, doi:10.1016/j.jastp.2010.05.007.

- Paper III (Appendix C: page 71)
  Placke, M., P. Hoffmann, M. Gerding, E. Becker, and M. Rapp (2013), Testing linear gravity wave theory with simultaneous wind and temperature data from the mesosphere, *J. Atmos. Solar Terr. Phys.*, *93*, 57–69, doi:10.1016/j.jastp.2012.11.012.

- Paper IV – Unpublished manuscript (Appendix C: page 85)
  Placke, M., P. Hoffmann, M. Rapp, R. Latteck, and E. Becker (draft prepared for submission), Mesospheric gravity wave momentum fluxes from radar measurements at polar latitudes in comparison with model results.

Danksagung

An dieser Stelle möchte ich mich sehr herzlich bei Prof. Dr. Markus Rapp bedanken, der mir die Bearbeitung dieses Promotionsthemas ermöglichte und mir als mein Hauptbetreuer bei dieser Arbeit stets viele anregende Ideen und sehr gute Hilfen zum erfolgreichen Vorankommen und Gelingen gab. Ebenso gilt mein besonderer Dank meinem Zweitbetreuer Dr. Peter Hoffmann, der mir immer sehr engagiert bei all meinen Fragen und Anliegen weiterhalf und mich bei umfangreichen Datenauswertungen und Programmverbesserungen tatkräftig unterstützte. Diese beiden Wissenschaftler standen mir stets mit Rat und Tat zur Seite, selbst nachdem Prof. Dr. Markus Rapp seinem Ruf an das IPA des DLR in Weßling-Oberpfaffenhofen folgte und Dr. Peter Hoffmann in den Ruhestand ging. Von ihnen konnte ich mir außerdem unschätzbares Wissen zum erfolgreichen Schreiben von wissenschaftlichen Veröffentlichungen und Gutachten sowie zum Erstellen von gut strukturierten Vorträgen und Postern für Konferenzen und Workshops aneignen. Weiterhin danke ich Prof. Dr. Franz-Josef Lübken für die kritischen und konstruktiven Anmerkungen zu meiner Arbeit bei diversen Workshops und Seminaren. Danke auch für die Möglichkeiten, meine Ergebnisse auf nationalen und internationalen Konferenzen präsentieren und diskutieren zur können und somit meinen eigenen wissenschaftlichen und kulturellen Horizont zu erweitern. In diesem Zusammenhang möchte ich auch dankend erwähnen, dass ich am Aufbau des MAARSY-Radars auf Andøya in Nordnorwegen aktiv beteiligt sein durfte und so die Möglichkeit bekam, einen kleinen Einblick in den Aufbauprozess und die Komplexität eines der größten Atmosphärenradarsysteme der Welt zu erlangen. Außerdem konnte ich mir nebenbei ein Bild von allen sonstigen dort positionierten Radargeräten, deren Messdaten ich z. T. für meine Auswertungen verwende, und den optischen Instrumenten am ALOMAR-Observatorium machen. Weiterhin bedanke ich mich sehr bei allen Wissenschaftlern, die neben meinen Betreuern zum erfolgreichen Gelingen meiner Arbeit und den Veröffentlichungen der Ergebnisse beigetragen haben, insbesondere Prof. Dr. Erich Becker, Dr. Michael Gerding, Prof. Dr. Christoph Jacobi (Institut für Meteorologie, Universität Leipzig), Dr. Gunter Stober und Dr. Ralph Latteck. Ich danke den Mitarbeitern der Abteilung ”Radarsondierungen und Höhenforschungsraketen” und allen anderen Mitarbeitern des IAP für die sehr gute Zusammenarbeit sowie die sehr freundliche und angenehme Arbeitsatmosphäre. Zu guter Letzt möchte ich mich recht herzlich bei meiner Familie und meinen engsten Freunden bedanken, die mir stets Rückenhalt gaben, mit mir über (vermeintlich) große und kleine Probleme diskutierten und mich beruflich und privat motivierten.

Erklärung über den Eigenanteil an den Manuskripten

Die in dieser kumulativen Dissertation eingebundenen Veröffentlichungen *Placke et al.* (2011a, b, 2013) und das bislang unveröffentlichte Manuskript wurden von Frau Manja Placke verfasst. Dabei wurden wenige zugearbeitete Textpassagen von den Co-Autoren beigetragen, die auch bei der anschließenden Überarbeitung mitwirkten. Ebenso hat Frau Placke die gezeigten Grafiken bis auf wenige Ausnahmen selbst erstellt und die zugrunde liegenden Daten verarbeitet.

In *Placke et al.* (2011a) hat Frau Placke für die Auswertung der Meteorradardaten hinsichtlich Winden, Windvarianzen und Impulsflüssen grundlegende Analysemethoden, die in den Veröffentlichungen von *Hocking et al.* (2001) und *Hocking* (2005) vorgestellt wurden, programmiertechnisch umgesetzt. Diese Methoden wurden auf die aus Rohdaten routinemäßig abgeleiteten Meteorpositionsdaten eines Meteorradars angewandt. Dabei hat Frau Placke einzelne Kriterien zur effektiven Selektion der Daten gewählt und kritisch überprüft. Ideen zur Windscherungskorrektur und zur jährlichen Variation von Wind- und Windvarianzen wurden von Prof. Dr. Christoph Jacobi beigetragen. Die Datenverarbeitung hat Frau Placke selbstständig durchgeführt. Der Eigenanteil von Frau Placke an dieser Veröffentlichung beträgt etwa 80%.

In *Placke et al.* (2011b) wurden die in der vorangegangenen Veröffentlichung genutzten Analysemethoden in einer Sensitivitätsstudie auf ihre Anwendbarkeit überprüft. Dafür wurden prozessierte KMCM-Modelldaten (4-dimensionale Windfelder) von Prof. Dr. Erich Becker zur Verfügung gestellt, die Frau Placke mit eigenen Analyseprogrammen für ihre Anwendungszwecke weiterverarbeitet hat. Zusätzliche Analysen bezüglich Winden, Windvarianzen und Impulsflüssen in mittleren und polaren geographischen Breiten wurden von Frau Placke mit weiteren Meteorradardaten durchgeführt. Ihr Eigenanteil an dieser Veröffentlichung beträgt etwa 85%.

In *Placke et al.* (2013) nutzte Frau Placke die oben genannten prozessierten KMCM-Modelldaten vom Windfeld sowie zusätzlich vom Temperaturfeld, um die lineare Schwerewellentheorie zu verifizieren. Für deren experimentelle Überprüfung wurden Winddaten des MF-Radars in Juliusruh von Dr. Peter Hoffmann und Temperaturdaten des K- und RMR-Lidars in Kühlungsborn von Dr. Michael Gerding zur Verfügung gestellt. Die Datenauswertung wurde von Frau Placke durchgeführt, wobei bei der Hodographen- und Stokesparameteranalyse Dr. Peter Hoffmann Zuarbeit geleistet hat. Der Eigenanteil an dieser Veröffentlichung beträgt etwa 75%.

In dem bislang unveröffentlichten Manuskript hat Frau Placke routinemäßig erzeugte Ergebnisse der Doppleranalyse des MF-Radars in Saura verwendet. Für die Berechnung des Wind- und Impulsflussfeldes wurden die in *Vincent and Reid* (1983) veröffentlichten Analysemethoden verwendet. Auch hier hat Frau Placke Kriterien zur Selektion der in die Analyse einfließenden Daten eigenständig gewählt und überprüft und die Wind- und Impulsflussdaten ausgewertet. Zudem wurden prozessierte KMCM-Modelldaten vom Wind- und Impulsflussfeld für weitere Auswertungen genutzt. Der Eigenanteil von Frau Placke an dieser Veröffentlichung beträgt etwa 90%.

Kühlungsborn, den 19. September 2013

(Manja Placke)

Selbstständigkeitserklärung

Hiermit versichere ich an Eides statt, dass ich die vorliegende Arbeit selbstständig angefertigt und ohne fremde Hilfe verfasst habe, keine außer den von mir angegebenen Hilfsmitteln und Quellen dazu verwendet habe und die den benutzten Werken inhaltlich oder wörtlich entnommenen Stellen als solche kenntlich gemacht habe.

Die Arbeit wurde bisher weder im Inland noch im Ausland in gleicher oder ähnlicher Form einer anderen Prüfungsbehörde vorgelegt. Weiterhin erkläre ich, dass ich ein Verfahren zur Erlangung des Doktorgrades an keiner anderen wissenschaftlichen Einrichtung beantragt habe.

Kühlungsborn, den 19. September 2013

(Manja Placke)